EUROPEAN ORGANIZATION FOR NUCLEAR RESEARCH

CERN-EP/85-80
23 May 1985

PROPERTIES OF A FINE SAMPLING URANIUM-COPPER SCINTILLATOR HADRON CALORIMETER

T. Akesson, R. Batley, O. Benary, J.C. Berset, O. Botner, M. Burns, W.E. Cleland, S. Dagan, P. Dam, G. Delavallade, A. Di Ciaccio, G. Di Tore, C.W. Fabjan, H.A. Gordon, M. Harris, P.W. Jeffreys, G. Kesseler, J. Lindsay, D. Lissauer, W. Molzon, B.S. Nielsen, L. Olsen, Y. Oren, J. Renaud, L. Rosselet, R. Schindler*), I. Stumer, J. v.d. Lans, E. Vella, C.J. Wang, R. Wigmans, W.J. Willis, M. Winik, W. Witzeling and C. Woody

CERN, Geneva, Switzerland

ABSTRACT

We present results obtained with a uranium/copper scintillator fine-sampling calorimeter with wavelength shifter readout. Test beam measurements made with $e^{\pm}$, $\pi^{\pm}$ and protons in the momentum range 0.3 to 40 GeV/c are presented. The calorimeter achieves energy resolutions of $\sigma(E)/E = 0.36/\sqrt{E}$ and $0.16/\sqrt{E}$ for hadrons and electrons, respectively. The measured ratio of response for electrons to that for hadrons is 1.11, for energies of 2 GeV or more. The spatial resolution achieved for single particles at normal incidence is $\sim$ 1 cm for electromagnetic showers and $\sim$ 3 cm for hadronic showers. Operational experience over three years of running at the CERN ISR, including operation at very high luminosities ($\sim 1.4 \times 10^{32}$ cm^{-2}s^{-1}), is described.

Submitted to Nuclear Instruments and Methods in Physics Research

---

* Present address: California Institute of Technology, Pasadena, California

1. INTRODUCTION

Several reasons contribute to the increasing use of hadronic calorimeters in elementary particle physics:

i) In many experiments reactions between constituents are studied, manifesting themselves as collimated 'jets' of particles. Both the high density of particles and the large neutral component of jets can best be measured with calorimetric techniques.

ii) The accuracy of calorimetric energy measurement relatively to magnetic momentum analysis improves with increasing energy. The 'crossover' is frequently reached in experiments operating at present accelerators.

iii) Calorimeters provide unique advantages for sensitive event selection at the trigger stage, which may be crucial for successful experimentation at high-interaction rate p-p or e-p colliders.

We describe here the construction and performance of a large hadron calorimeter which was operated for several years at the CERN Intersecting Storage Rings (ISR) as part of the Axial Field Spectrometer (AFS) [1] (Fig. 1). The physics programme emphasized the study of hard scattering of proton constituents, manifesting itself in the production of single high-p_T hadrons, prompt photons, very large E_T events, or 'jets' of particles [2]. The existence of jets was in fact an unresolved issue at the time of the construction of the AFS. The choice of a hadron calorimeter as an essential component of this spectrometer was strongly motivated by points i) and iii). In the central rapidity region at the ISR, the secondary particles are produced with relatively low average energy, and the cross-section decreases very steeply with transverse momentum p_T ($dN/dp_T \sim p_T^{-n}$, $n \simeq 6$-10); this p_T-spectrum imposed very stringent requirements on the quality of the instrument [3]:

a) The measured p_T spectrum is strongly distorted if the energy resolution is poor; this affects also the performance of triggers sensitive to energy deposit in the calorimeter, which tend to be satisfied predominantly by events whose true energy is below the threshold but whose measured signal fluctuates upward;

b) In general, hadron calorimeters have very different responses towards neutral and charged pions, making the triggering on and measurement of particles and jets very problematic, particularly at ISR energies.

A considerable improvement in performance is obtained by using uranium-238 as the passive absorber material in a sampling calorimeter [4]. Interactions between the hadrons of a hadronic cascade and the nuclei of the calorimeter tend to suppress the 'visible' hadronic energy relative to the energy from a purely electromagnetic cascade, whence the unequal response to neutral and charged pions. Partial or complete compensation of these 'nuclear' losses may be achieved in ^{238}U absorbers, as the relatively energetic neutrons (1-10 MeV), characteristic of the nuclear break-up processes, induce a correlated number of fissions. These in turn contribute to the measured signal (through recoil reactions of neutrons with the active medium or Compton scattering of the fission photons). In addition, there is evidence that the use of high-Z absorbers reduces the relative response of the electromagnetic component of hadron showers contributing also towards the equalization of response [4]. A nearly identical response to charged and neutral pions, leading to an intrinsic energy resolution of $\sigma(E)/E \simeq 0.22/\sqrt{E(GeV)}$, has been measured for a uranium calorimeter [5]. This should be compared to an intrinsic resolution of $\sigma(E)/E \simeq 0.45/\sqrt{E(GeV)}$ typical of a non-compensated calorimeter.

In the construction of the AFS calorimeter a number of sometimes conflicting requirements had to be satisfied. We list below the most important of these requirements.

i) Identical response to hadrons and electrons: the use of uranium is the only established method to achieve this.

ii) Very good hadron resolution: also achieved by the use of uranium. We chose 3 mm thick uranium plates for the hadron absorber, which contribute sampling fluctuations of $\sigma(E)/E \simeq 0.20\%/\sqrt{E}$ (GeV), equal to the intrinsic resolution [5]. This choice is a compromise between the conflicting demands of small sampling fluctuations (i.e. many thin plates) and minimum average absorption length λ (few U plates and fewer active readout layers). Of course, the cost of uranium processing is also reduced.

iii) Good transverse granularity: the requirements depend on the characteristic angular dimensions of the event topology under study, the average transverse shower diameter d in the calorimeter ($d \sim \lambda$), and the distance D of the calorimeter from the collision. As the design criterion for the AFS calorimeter, the granularity was chosen such that the majority of particles inside a 'jet' would be resolved. With a $\langle\lambda\rangle \sim 20$ cm and the calorimeter at a distance $D \simeq 120$ cm, a tower size of 20 x 20 cm² meets this requirement.

iv) Electron identification: achieved by means of a measurement of the longitudinal shower distribution. In our design, each tower is subdivided into an electromagnetic front section of 6 radiation lengths (X_0) and a hadronic absorber of 3.8 absorption lengths (λ).

v) Uniformity of response and control of systematic effects at the few percent level: this requirement affects the choice of the signal readout, for which we considered both a liquid argon-(LAr) ion-chamber readout [5] and a scintillator/wavelength shifter system. From tests we concluded that the performance of the latter solution was adequate for the ISR application and for that reason preferable to the LAr readout, which would have required a mechanical construction of considerably greater complexity. The construction was simplified by arranging the towers in a square non-projective geometry, which improves the uniformity of the readout system and minimizes the energy lost in cracks between modules.

vi) Ability to trigger on various event topologies (single particles, jets, electrons, ...) with a quality commensurate with the off-line performance of the instrument, and with a selectivity and trigger speed adapted to the interaction rate of the ISR: the energy information for trigger purposes must therefore correspond to the 'physical' energy of the particles, which implies certain restrictions in the layout and signal treatment of the device [6].

We present first the calorimeter construction details, explain the choice of uranium/copper mixture, and examine in detail the performance of the optical readout system. Energy calibration is discussed next. Test beam results are presented showing the response as a function of energy,

particle type, and angle of incidence. We present a detailed comparison between electromagnetic and hadronic response. A Monte Carlo program used to simulate the calorimeter response to single particles and jets is described. We conclude with a discussion of experience gained while operating the calorimeter for three years at the CERN ISR.

2. CONSTRUCTION

2.1 Mechanical construction

An isometric view of the calorimeter is shown in Fig. 2. The calorimeter provides a total coverage of 8.55 sr, 2π in azimuth and approximately ± 0.85 in pseudo-rapidity. Each of the four walls is composed of 2 x 16 stacks. Each stack (Fig. 3 and Fig. 4) is subdivided into six towers with surface areas of 20.0 X 20.8 cm^2, resulting in a matrix of 12 x 16 towers per wall. The towers have four-fold wavelength-shifter (WLS) readout: right and left, at each of two depths. The photo-multiplier dynode signals provide energy information for trigger purposes, whereas the anode signals provide energy information for the off-line analysis.

The four walls are arranged to overlap with approximately 3 X_o at the corners to insure an uninterrupted e.m. layer of uranium calorimetry (the horizontal calorimeters are located at a distance of 116 cm and the vertical ones at 120 cm from the nominal beam crossing). In these four corners, there is (on average) a few percent of the hadronic energy of an event, which is measured with Cu/scintillator calorimeters having hadronic resolution $\sigma(E)/E = 0.48/\sqrt{E}$ [4]. This arrangement reduces the total amount of uranium required without compromising the energy resolution.

The absorber volume (80 cm deep) of a stack is divided into two parts longitudinally. The e.m. front part consists of ten 2 mm thick uranium plates (a total of 6 X_o). The hadronic part consists of 3 mm thick uranium plates and 5 mm thick copper plates mixed in the ratio 2:1, arranged as shown Fig. 4 (3.8 λ). Two consecutive metal plates are interleaved with a 2.5 mm thick scintillator plate. The gap width between two metal plates is 3 mm, ensured by 5 brass spacers located in holes in the scintillator plates. A 60 μm thick sheet of polyester paper on

either side protects the scintillator against scratching by the metal plates. Table 1 summarizes the mechanical properties of a stack.

An aluminium I-profile serves as a rigid support structure for the stack and the photomultipliers. A central tie rod and two end-plates mechanically constrain the stack (Fig. 3). This construction has been chosen to minimize the mechanical support structures, which would introduce dead areas and non-uniformities in the light collection. As a consequence, however, the stacks are self-supporting and mechanically stable only in the positions used in the experiment (Fig. 2) and require special equipment for handling and transport.

The uranium plates are depleted to approximately 99.6% of ^{238}U*). The plates were produced by a rolling operation starting from ingots of various shapes. In the first stage these were kept annealed during the rolling until a thickness of $\sim$ 4 mm was achieved. The final reduction to the nominal thickness was done by 'cold' rolling, which produced a rather smooth surface. These plates were then sheared to size and one central hole was punched. The burrs left by these operations were sufficiently small as to require no further treatment. The surface quality produced by the cold-rolling was sufficiently inert to oxydization that no further surface treatment was required. Handling and assembly were carried out in a restricted work zone with radiation monitors for dust and radon emanation. Apart from the use of full-body overalls and gloves, and regular health-physics checks, no further restrictions had to be imposed on the assembly crew [7]. The monthly dose rate received by the workers was typically 40 mrem, and it never exceeded 60 mrem.

2.2 The readout system

Our choice of the active readout system was governed by the following considerations:

- The instrumental errors on the energy measurement should not impair the intrinsic performance of the calorimeter. With energy deposits in the 30-40 GeV range and corresponding measurement errors of $\sim$ 5%, additional instrumental effects contributing to the energy resolution

---

* Supplied by Rocky Flats Plant of Rockwell International, Denver, CO, USA

need to be controlled at the 2-3% level. Overall calibration errors affecting the energy scale need to be monitored even more precisely.

- Provision for adequate transverse and longitudinal subdivision.
- Rate capability adapted to the ISR environment of $\sim 10^6$ collisions/sec.

Table 1

Mechanical properties of an AFS Calorimeter Stack

Electromagnetic front section	
Number of U plates	10
Size of U plates	1200 x 204 x 2 mm³
Number of scintillator plates	10
Size of scintillator plates	1198 x 205 x 2.5 mm³
Number of optical channels	12 (6 right, 6 left)
Hadronic back section	
Number of U plates	76
Size of U plates	1200 x 200 x 3 mm³
Number of Cu plates	38
Size of Cu plates	1200 x 200 x 5 mm³
Number of scintillator plates	114
Size of scintillator plates	1198 x 201 x 2.5 mm³
Number of optical channels	12 (6 right, 6 left)
Weight of complete stack	approx. 2200 kg
Overall depth of a stack with PMTs	1337 mm
Total number of stacks in AFS	128

(plus 64 copper/scintillator calorimeters covering the corners).

We adopted a scintillator/WLS readout system [8]. The scintillator is based on PMMA (polymethyl methacrylate) [9] and has the following composition: PMMA 89%, naphthalene 10%, butyl-PBD 1%. This'plastic' scintillator*)

* produced by Altulor, Paris, France

was chosen because of its considerably lower price and its superior mechanical properties, relative to the more 'conventional' organic scintillators. The level of naphthalene admixture was a compromise between light output (Fig. 5) and mechanical softness, both of which increase with increasing naphthalene content. We purposely did not add a secondary wavelength shifting agent to the scintillator to shift the light towards longer wavelengths, as is commonly done, to achieve the following properties: the emission spectrum of butyl-PBD peaks at 368 μm, well matched to the absorption of the WLS (Fig. 6). The scintillator, when used in conjunction with the WLS, is measured to have an optical attenuation length $\lambda_{opt} \sim 35$ cm; this, for our small cell width, is close to optimum and permits shower localization by comparison of the signals read out on the two sides. There is a further reason for opting for a very high light attenuation: the six-tower structure per stack was achieved by a sixfold optical readout with six 20 cm wide WLSs on each side of a stack, but without a mechanical subdivision of the scintillator sheets (see Table 1). This was done to facilitate the mechanical assembly. The short attenuation length and solid angle effects in the light collection provide an effective segmentation. With this arrangement, approximately 60% of the light produced by a shower is measured in a tower struck centrally by the incident particle, while 15% are measured in each of the adjacent towers and the remainder in the next-to-adjacent ones. Particular care had to be exercised to ensure an approximately identical response for the 'end'- towers of each stack, achieved by judicious polishing of the scintillators and by placing an aluminium foil reflector at the ends. The edges of the scintillators viewed by the WLS were diamond-cut, but not further polished.

The performance of the WLS readout depends critically on a careful optimization of the scintillator-WLS-photomultiplier (PM) combination. We selected BBQ (benzimidazo-benzisoquinoline-7-one), with an emission spectrum peaked at $\sim$ 500 nm, as the fluorescent chemical*) (see Fig. 6).

---

*) WLS plates doped with POPOP have also been tested. POPOP has a fast fluorescence decay time and its emission spectrum is better matched to standard photocathodes. Nevertheless, the resultant light yield is essentially the same as for BBQ-doped WLSs because the absorption of POPOP matches badly the emission of butyl-PBD. Further problems arise from the fact that the POPOP absorption spectrum is located in the blue, making the device more sensitive to Cherenkov light produced in the WLS plates.

The concentration of this chemical has to be optimized in two respects: the absorption efficiency for the incoming scintillator light should be high, and the self-absorption for the re-emitted light, which has to travel along the WLS towards the PM, should be small. Both quantities rise with increasing concentration of BBQ. An undesired feature of WLS plates is their sensitivity to Cherenkov light. When the shower develops near the edge of a calorimeter unit, part of it will extend into the WLS. The Cherenkov light produced by electrons in the shower is converted by the fluorescence mechanism and cannot be distinguished from the scintillator light. If the fraction of signal due to Cherenkov light becomes significant, the uniformity of response of the calorimeter will be badly influenced. Use of thin WLS plates is one obvious way to reduce this effect. The limit is given by the tolerable longitudinal attenuation in the WLS, adversely affected by the larger BBQ concentration and the increasing number of internal reflections, before the light reaches the end of the plate. Our measurements showed a significant increase of attenuation for plates of 1 and 1.5 mm thickness, compared with samples of 2, 3, and 4 mm. A further reduction of the Cherenkov effect was obtained by doping the WLS material with an ultraviolet absorbing (UVA) chemical, absorbing part of the Cherenkov light before it is converted by the BBQ, as illustrated in Fig. 7.

After extensive optimization tests, we adopted a composition of 80 mg/l BBQ in 2 mm thick Plexiglas 201*) bars containing a certain (to us not specified) concentration of UVA: Fig. 8 illustrates the uniformity obtained with two WLS plates, both doped with the same concentration of BBQ but differing in thickness and in UVA concentration. The attenuation along the WLS (a combination of bulk attenuation and losses due to surface imperfections) is of course undesired, as the light output changes according to the position of its conversion. This was improved by the application of a diffuse end reflector, a white paint (Diegel 05197 HVZ) with a very good adherence to acrylics. The resulting attenuation is shown

---

* We are indebted to Drs. Fischer and Kretz of Röhm GmbH, Darmstadt, Fed. Rep. Germany, for their kind assistance and the provision of numerous samples.

in Fig. 9. The level of ∿ 10% non-uniformity is tolerable for our range of energy measurements. It is worth-while to note that this level of uniformity is to a certain extent fortuitous since the light losses due to bulk attenuation are partially compensated by reflection from the edges of the WLS.

The light from the WLS was guided to the PM by means of a light-guide of the lamella type. It was essential to make the light guides from ultraviolet-absorbing acrylic glass in order to reduce the Cherenkov light produced by particles crossing the light-guide. In addition, a 3 mm thick disk of elastic silicone rubber doped with a UVA chemical *) provided the optical coupling between light-guide and PM. The disk acts as a UV filter with an absorption edge at ∿ 390 nm. This optical readout produces approximately 1.5 photoelectrons per minimum ionizing particle and per scintillator (∿ 150 photoelectrons in total for a minimum ionizing muon).

The photomultipliers (Table 2) were operated with a semi-linear voltage divider drawing approximately 1 mA. A printed-circuit board soldered to the socket carried all the components, to which also three equal-length coaxial cables (type RG 178) were connected. The 24 anode cables of a given stack were collected onto two AMP CPC (24) connectors mounted in a metallic box on the back of the stack. A 100 m long cable, containing 12 coaxial cables RG 58, was used to bring the signal to the counting room. A similar cabling arrangement was adopted for the high voltage supply. The 24 high voltage leads were connected to an AMP CPC (37) connector, housed in a metallic box. From each stack a shielded, 28-conductor cable connected the stack to the high voltage supply, located in the counting room. On the counting room side, a printed-circuit patch panel was soldered to the RG 58 cables to serve as a transition to the flat coaxial cables which were connected to the ADCs**). The PM dynode cables were connected and summed over polar angles at constant azimuth (48 sums). The e.m. and hadronic dynode signals were separately grouped into AMP (36) connectors on 'summing' amplifiers, the outputs of which were transmitted via aircore cables (ß = 0.95) to the trigger processor in the counting room.

---

* Tinuvin P, Ciba-Geigy, Basel, Switzerland.
** Charge integrating ADCs, type LeCroy 2282B or type 2282A modified.

The PMs had to operate in the stray field of the 'Open Axial Field Magnet' [1], which at certain locations reached values up to 0.12 T. Three shields*) were used: the outer shield was made from softmagnetic iron (type ST28), the middle one from a nickel-iron (50/50) alloy (type Permenorm 5000) and the innermost is a mu-metal cylinder, which was kept at cathode potential through a copper-beryllium spring soldered to the PM base.

Table 2
Photomultiplier characteristics

PM type	Philips XP 2008/UB
Socket type	FE 1112
Cathode diameter	1.5" (38 mm)
Cathode type	Super-A (similar to S-11)
Multiplier	10 stage semi-linear focusing
Maximum operating voltage	1800 V
Maximum average current	200 μA d.c.
Typical operating voltage	1200-1600 V for a gain of $\sim 10^6$

2.3 Systematic effects in the readout system (a general discussion)

We have indicated that the performance of the optical readout did not influence the performance of the calorimeter significantly. This was due to the relatively low energy of particles, < 15 GeV/c, to which the calorimeter towers were exposed. However, these conclusions are reversed when considering the use of such instruments for fixed target applications or at the higher-energy colliders, in existence or planned. This can be best seen by considering the performance as a function of the optical uniformity of both the scintillator and the WLS. In Fig. 10a we show the resolution $\sigma(E)/\sqrt{E}$ versus energy for electrons for different values of the attenuation length λ of the scintillator. The value of λ = 34.1 cm corresponds to the attenuation of scintillators which were never used in a calorimeter stack (measured on five year 'old' scintillator, but comparing rather closely to a related measurement done immediately after production). Scintillator taken from a stack, which was used in the ISR for 30 months and which is estimated to have received a dose of < 10^4 rad (mostly from the radioactivity background of the uranium plates) has been measured

*) Supplied by Vacuum Schmelze GmbH, Hanau, Fed. Rep. Germany.

to have an attenuation length of 15.2 cm, whilst scintillator exposed to a dose about twice as large has degraded to λ = 11.3 cm. In Fig. 10b, a similar evaluation is done for hadronic showers.

The effect of WLS non-uniformities is evaluated in Figs. 11a and b. The results are given in terms of the 'effective' optical attenuation length λ_{opt} as measured in an actual geometry. We conclude that λ_{opt} has to be larger than $\sim$ 3 m to avoid the introduction of a substantial worsening of the resolution at energies > 100 GeV. It is interesting to note that the WLS which received doses of $\sim 10^4$ rad showed no measurable decrease in the attenuation length.

It is important to realize that even relatively low doses of 10^4 rad can cause dramatic damage, if the dose rate is very low, e.g. due to the uranium radioactivity. Measurements [10] carried out at much higher dose rate indicated that integral doses in excess of 10^5 rad could be tolerated for the scintillator used in this calorimeter. We believe that the radiation damage is caused by O_2^* molecules, excited by the UV-component of the scintillation light. The same scintillator shows order-of-magnitude higher resistance to radiation when kept in an inert atmosphere [11].

3. CHOICE OF URANIUM/COPPER MIXTURE

A series of tests were carried out to study the sensitivity of the energy resolution to the thickness of the absorber plates and to the possible admixture of non-uranium plates (we used copper to avoid distortions of the magnetic field of the spectrometer). The plates in U calorimeters have to be made quite thin, so that sampling fluctuations do not dominate the intrinsic energy resolution. In the absence of instrumental effects, the total energy resolution in a sampling calorimeter (at 1 GeV) may be expressed in the form [3]

$$\sigma^2_{resol} = \sigma^2_{intrinsic} + \sigma^2_{sampling},$$

where $\sigma_{intrinsic} = 0.22$ and the sampling component is

$$\sigma^2_{sampling} = 0.09^2[\Delta E\ (MeV)],$$

for hadronic showers, where ΔE represents the energy loss of a single charged particle in one cell (absorber plate plus scintillator plate). A lower bound on the resolution is estimated as σ (2 mm plates) = 28.6% and σ (3 mm plates) = 31.4%. The expected improvement using 2 mm instead of 3 mm plates is relatively small, which was confirmed by tests (Table 3).

Three U/Cu mixtures were tested in addition to a pure copper stack made with 5 mm plates to evaluate the effect of non-U absorbers on the performance. In each case the stacks had approximately the same total depth (in nuclear absorption lengths). The results reported in Table 3 are averaged over incident momenta of 2-10 GeV/c. At the higher momenta, leakage occurred for the hadronic showers. Thus a 'truncated' Gaussian fit was made to the energy distribution, between a point at 50% of the peak height on the low edge and 15% of the peak height on the high edge. This procedure was checked in the test beam by installing a second layer of stacks to measure back-leakage. The truncated mean was shown to minimize the effect of leakage, and gave results consistent with total containment measurements. As one example, the distribution measured for 4 GeV/c pions is shown in Fig. 12. One notes that the distribution is Gaussian over more than two orders of magnitude.

The results quoted in Table 3 indicate that a moderate copper admixture does not seriously affect the performance of the calorimeter, but that with increased copper content the resolution and the response of hadrons relative to electrons approach the performance of a non-compensated device. As a compromise on the number of uranium plates and the total tonnage of uranium we adopted configuration 4 of Table 3, and all subsequent discussions refer to this choice.

4. ENERGY CALIBRATION AND GAIN BALANCING

Probably the most difficult task in high-quality calorimetry concerns the absolute and relative energy calibration. Optical readout methods, in particular, suffer critically from non-uniformity in the light collection and ageing of the optical components, which affect both the energy scale and the relative response of different calorimeter segments.

Table 3

Characteristics of the U/Cu calorimeters

No.	Configu-ration (U:Cu mix)	No. uranium plates (2 mm)	(3 mm)	Copper plates (5 mm)	Absorpt. lengths (λ)	Radiation lengths (X_o)	Resolution $\sigma \cdot \sqrt{E}$ (%) electrons	hadrons	Ratio * e/h
1	1:0	162	-	-	3.65	102.4	13.9 ± .3	33 ± 1	1.12
2	1:0	10	125	-	4.23	124.4	16.2 ± .3	33 ± 1	1.11
3	4:1	10	95	22	4.07	103.9	15.8 ± .7	35 ± 1	1.09
4	2:1	10	76	38	4.05	91.3	15.9 ± .3	36 ± 1	1.11
5	1:1	10	53	53	3.86	75.3	15.1 ± .3	38 ± 1	1.22
6	0:1	-	-	100	3.66	35.7	13.2 ± .7	48 ± 1	1.48

* The e/h ratio is quoted for the measured energy deposits for electrons and pions and is not corrected for the energy leakage of pion-induced showers.

These problems are partially alleviated in a uranium calorimeter, because the U radioactivity acts as a convenient, stable, built-in method of relative calibration of the complete optical readout chain. In our instrument, we measured that the radioactivity-induced light, integrated over 10 μsec, corresponds to the light produced by an energy deposit of 0.4 GeV in an electromagnetic PM (with an r.m.s width of 11%) and 3 GeV in a hadronic PM (with an r.m.s width of 5.6%).

We adopted the following sequence of steps for the absolute and relative calibration:

1) Several calorimeter modules were exposed to muons, electrons and hadrons of 2-10 GeV/c momenta in a test beam (described more fully in Section 5). On the basis of the calculated energy of muons in the e.m. and hadronic sections, the relative PM gain was balanced, and from then on maintained through the uranium radioactivity signal (measured absolutely in coulombs). Once all channels had been equalized, the absolute energy scale was established with electrons, and maintained on the basis of the measured U radioactivity. This relation is of course calorimeter-specific and depends on other factors besides the sampling ratio of active to passive layers.

The relative balancing of the front and back sections of a calorimeter tower was carried out in the following way. A 4 GeV beam of muons was directed into a calorimeter stack. The front and back energy distributions were fitted to a Vavilov distribution [12] and fits were then used to derive the most probable pulse heights. These were scaled to the theoretical most probable energy losses calculated for each section. With the weightings established in this way, the calorimeter proved to be linear and the response was independent of angle (despite the greater projected thickness of the plates at non-normal incidence). The ratio of the average energy deposited in the e.m. part to that in the hadronic part for electrons at 5 (10) GeV is 42% (36%) in agreement with predictions from the EGS Monte Carlo program [13]. Failure to balance the two parts would result in two effects for e.m. showers: non-linearity of response and variation of resolution as a function of energy and angle.

The absolute energy calibration with electrons was only carried out for a few calorimeter modules. The same electron/muon ratio was assumed to apply to all the remaining modules, as discussed in the next step.

2) In the subsequent step, each tower of each stack was once calibrated with cosmic-ray muons. Its response was monitored and compared to the 10 μsec radioactivity signal measured absolutely in coulombs. The calibration constants (muon peak [MeV]; U radioactivity [coulomb]) for all 768 towers were clustered in a rather narrow distribution with width $\sigma \simeq$ 2.5%. The width of this distribution indicates the degree of accuracy of this calibration method, and also that other radioactive impurities in the uranium were not affecting it. During the subsequent ISR operation the response of the calorimeter was maintained constant by adjusting the phototube HVs to maintain the radioactivity-induced current at a fixed reference level.

One should note that exposure of a calorimeter to relativistic muons alone does not permit to establish an absolute energy scale. Let S_μ be the signal recorded from relativistic muons corresponding to their most probable energy loss ΔE_μ[GeV], as obtained with the procedure described under point (1); an energy deposit of 1 GeV would then result in a calorimeter signal of $C_\mu[1\ \text{GeV}] = S_\mu/\Delta E_\mu$. Likewise, let S_e be the signal recorded from an electron of kinetic energy E (GeV) and therefore $C_e[1\ \text{GeV}] = S_e/E$, the corresponding signal at 1 GeV. In the device described here, we performed the measurement with 4 GeV/c electrons, and muons, and obtained for the so-called "μ/e"-ratio

$$C_\mu/C_e = 1.26 \pm 0.01.$$

Such deviations from the 'naïve' muon calibration have been reported previously [4].

5. TEST BEAM STUDIES

5.1 Description of the apparatus

Five calorimeter stacks were placed side by side in a supporting frame and were exposed to a test beam at the CERN Proton Synchrotron (PS) and Super Proton Synchrotron (SPS). The support structure could be rotated about two orthogonal axes and translated in horizontal and vertical

directions, permitting the angle of incidence and the impact point to be varied. Time of flight measurements for protons and pions at 0.7 and 1.0 GeV/c were used to establish the beam energy scale and a lead-glass block was used to check the higher momentum settings of the electrons in the beam. Upstream material in the beam line (Cherenkov counter windows and trigger counters) limited the range of very low momentum measurements.

5.2 Energy response for hadrons

The linearity of the calorimeter was checked with electrons in the range 0.3 to 10 GeV, and the response was measured to be linear to better than ±1% (see Fig 13). Once the linearity of the calorimeter readout was established, it was possible to make a detailed study of the hadronic response. The results shown are fits made over the Gaussian part of the energy distribution (as in Fig. 12). Figure 14 shows the deviation from linear response and the resolution over the range 4-40 GeV. The curves are remarkably flat. The resolution, computed from the r.m.s. width and the peak of the Gaussian, does not deteriorate seriously even at 40 GeV, where the back- leakage is significant. Figure 15 displays the detailed response of the calorimeter in the range 0.2 to 4 GeV. The response to pions and protons is consistent at the same kinetic energy. The non-linearity between 0.2 and 1.5 GeV is the result of particles depositing a large fraction of the energy by ionization, before interacting with a target nucleus. (This explanation is corroborated by the fact that the hadronic energy resolution improves in this region.) This non-linear energy response effect is of course more pronounced for an uncompensated calorimeter (see also Section 5.4).

5.3 Gate length tests

The electron and hadron energy signals and resolutions were studied as a function of the ADC gate length, which was varied between 50 to 150 ns. Results for the energy deposit are given in Fig. 16. We attribute the rise in the measured electron signal with increasing gate length to the fluorescent decay time of the optical readout system, and in particular to the WLS bars.

The hadron signal rises more strongly with increasing gate length, indicating that the slow, fission-driven signal component has a time constant τ of $\sim$ 30 ns. This interpretation is consistent with the measurements of the gate-length dependence of the energy resolution (Fig. 17). Whereas for electrons the energy resolution is independent of gate length in the range 50-150 ns, the hadronic resolution is noticeably improved for measurement times long enough to exploit the fission compensation.

5.4 Comparison of e.m. and hadronic shower response

Figure 18 shows the ratio of e.m. to hadronic response as a function of the available energy of the particles. In our uranium calorimeter, high-energy electrons and pions produce nearly identical responses and their ratio has a plateau at a value of e/h $\sim$ 1.11 in the 2-10 GeV/c momentum range. The increased pion response below 2 GeV/c results from energy loss by ionization before a hadronic interaction takes place. A pion entering the calorimeter initially behaves like a muon, depositing energy by ionization for, on average, one absorption length before it interacts. At very low energies, most of the kinetic energy of the pion appears as ionization energy, which produces an enhanced signal in the calorimeter, comparable to that for muons, as discussed in Section 4. A Monte Carlo program (described in Section 6) incorporating the measured μ/e and e/h response ratios generates a curve which approximately reproduces the data (see Fig. 18).

In non-uranium calorimeters, electrons and pions produce a very different response above $\sim$ 2 GeV/c (e/h rises to $\sim$ 1.5). Below 2 GeV/c, mechanisms similar to those for compensated devices result in a non-linear response which, percentage-wise, is however considerably larger. (e/h changes from $\sim$ 1.5 to $\sim$ 0.7). Representative information on this behaviour is summarized in Figure 19.

Although the electromagnetic and hadronic response for the uranium calorimeter is similar in terms of visible energy, the shower development is different, allowing the identification of isolated showers. Figure 20 shows the rejection provided against pions for a fixed electron acceptance of 75%. At low energies this rejection is obtained entirely from the different longitudinal developments, whilst at high energies it is based equally on longitudinal and transverse information.

5.5 Spatial and angular dependence of response

A particle entering the centre of a tower at normal incidence will produce light in adjacent towers of the same stack through light coupling (see Section 2). For hadrons, energy will be also seen in adjacent stacks, owing to the lateral shower spread; its sharing will depend on the impact point and angle of incidence. Some care must thus be taken to collect light from towers adjacent to the 'struck' tower. We discuss results obtained with a '3-tower mask' (peak-energy tower plus the two adjacent ones in a stack) and a '9-tower mask' (peak-energy tower surrounded symmetrically).

5.5.1 Position resolution

A scan was made along the stack, to measure the position resolution and linearity across the face of the tower. The position is measured by comparing the pulse height in the two towers next to the peak tower. For electrons at normal incidence, a spatial resolution of $\sigma \sim \pm 1$ cm is measured (Fig. 21), while for hadrons it is $\sigma \sim \pm 3$ cm. The precision of the position measurement at the ISR is discussed in Section 7.4.

5.5.2 Response as a function of azimuthal angle of incidence

The uniformity of response as a function of ϕ (deviation from normal incidence relative to the long direction of a stack) is shown in Fig. 22. The small change for both energy and resolution between 14° and 22° is an artefact of the peak finding algorithm, because for $\phi > 22°$ the peak tower no longer coincides with the struck tower. In general one notes that it is necessary to consider a matrix of three by three towers to reconstruct the total energy and to recover the full energy resolution. In this case, the results are essentially independent of angle of incidence up to 45° with respect to normal incidence.

5.5.3 Response as a function of polar angle of incidence

In the polar direction (i.e. across a stack), the position is measured by using 'left' and 'right' information from the two sets of WLS bars of each tower. Figure 23 shows that the reconstructed position for electrons is remarkably well correlated to the true position (resolution $\sigma \sim \pm$ 1cm). Fig. 24 shows the energies recorded in two neighbouring towers A and B as a

scan is made with electrons across the face of the calorimeter. When the pulse heights from the two are added, a clear excess is seen when crossing the stack boundary. This, however, is the worst possible case; when the angle of incidence is $\theta = 40°$ the excess pulse height is reduced to less than 10%. Since hadron showers are much wider, the effect is much smaller, and even at normal incidence the effect is not measurable. This relatively good uniformity was achieved by careful tuning of the optical components, resulting in the rather good compensation of three effects: increase of light for showers close to the scintillator edge; emission of Cherenkov light for shower electrons in the WLS; and energy lost in the cracks. The remaining 15% non-uniformity can be further reduced with the following correction algorithm. Events within 2 cm of the edge of a stack can be identified because the position calculated across the stack (with a linear function) actually lies outside the physical dimensions of the calorimeter module, if the energy information from the neighbouring towers is also included. The distance beyond the limits of the stack is used in a third-order polynomial correction (dashed line in Fig. 24). Even in this worst possible case the correction works well. The energy response can thus be made independent of position and angles of incidence, although the energy resolution for electrons decreases by a factor of 2 over 10% of the acceptance, for normally incident electrons.

6. MONTE CARLO CALCULATIONS

6.1 General description

Two different approaches for simulation of showers as generated by particles in the calorimeter have been developed.

The first approach aims at a very detailed simulation of hadronic and e.m. showers to evaluate certain basic performance aspects [14]. For our studies, we have chosen a Monte Carlo procedure which has been maintained at CERN for several years [15]. This program, originally for use in neutrino experiments at BEBC, has later found wider applications in the study of shower development in extended blocks of material; it has ultimately been modified to describe the development of cascades in sampling calorimeters.

The main aim of the program is to follow, in the greatest possible detail , the propagation of a cascade induced by an incoming hadron, photon or electron. If the incident particle is a hadron, it is assumed to interact inside the detector at a depth determined by the absorption length generating a system of secondary hadrons. These in turn generate particles by further interactions, thus producing a particle cascade. For each interaction the Monte Carlo describes in detail how many particles of each kind are produced and the kinematics of each track, according to experimentally determined properties of the type of interaction in question. Each track is followed in a stepwise manner--verifying after every step whether an interaction occurred--until the momentum becomes so small that the track can be assumed to take no active part in the shower development.

If the incident particle is a photon or an electron, the processes responsible for particle production are pair production and bremsstrahlung. Also in this case the development of the cascade is followed step by step.

Whilst retaining the basic philosophy of this program, we have adapted it to the specific case of the AFS calorimeter. In particular, the possibility of fission subsequent to the interaction between a shower particle and a uranium nucleus has been considered, and the production of neutrons and photons resulting from such a process is incorporated. In addition, details of the calorimeter geometry and the readout system were introduced.

The program described above has been of considerable help when trying to estimate the effects on resolution and 'compensation' due to mixing uranium and copper plates in a calorimeter module. Later, the results of this program for the chosen U/Cu mixture were compared with results of beam tests and very good agreement was found [16].

For a number of studies, however, such a detailed and computer intensive procedure is not required, and a simpler shower simulation --parametrization of shower profiles-- was found to be adequate.

In this method, once the initial particle has interacted, the energy deposition due to the resulting cascade is described by an average shower profile [17]. The initial interaction distance d is distributed according to $f(d) = \lambda^{-1} \exp(-d/\lambda)$, where λ depends on the particle type, (the nuclear absorption length λ_0 for nucleons, $\sim 1.5\lambda_0$ for charged mesons, and the radiation length X_0 for electrons and photons). For a charged particle the ionization energy loss prior to interaction is calculated taking into account the $1/\beta^2$-dependence of the mean dE/dx. The ionization loss is scaled by the μ/e ratio (1.26), thus calibrating the signal to the energy scale appropriate for incident electrons. The deposition of the remaining energy $E = E_{incident} - (dE/dx)$, at a certain distance D from the interaction point, is then given by a two-component formula:

$$dE = E(Ax^{\alpha-1} e^{-x} dx + By^{\beta-1} e^{-y} dy)$$

where $x = D/X_0$ is the depth expressed in terms of radiation lengths, $y = D/\lambda_0$ is the depth expressed in nuclear absorption lengths, and A, B, α, β are energy-dependent parameters to be fitted by comparison to data. The first term in the above expression represents the 'electro- magnetic component' of a hadron-induced shower. For incident electrons and photons this is the only term (B = 0). For incident hadrons the integrated shower energy deposition is scaled by the e/h ratio (1.11), again calibrating the signal to the electron energy scale.

For the lateral development of showers, a two-dimensional Gaussian distribution is used where the variance is taken to be 0.5 of an 'average absorption length' ('average radiation length') for hadrons (electrons and photons).

After initial adjustment of the parameters, the procedure described above gives good agreement with test-beam data (Fig. 18). It requires considerably less computer time per particle, compared to the more detailed Monte Carlo method, an essential feature for a number of physics analysis projects.

6.2 Jet measurement with calorimeters: a Monte Carlo evaluation

One of the most interesting applications for hadron calorimeters is the energy measurement of multiparticle systems, in particular, jets of hadrons originating from fragmentation of individual partons (or from the colour field between partons). The AFS calorimeter has been used to measure jet cross-sections [2,18], to demonstrate jet dominance at high transverse energy [19] and to determine the jet energy and jet direction needed for fragmentation studies [20]. In this section, we will illustrate the performance of this calorimeter as a jet detector with a Monte Carlo study and compare it to the performance of a copper calorimeter described in Ref. [4]. For this Monte Carlo evaluation we use the previously described hadronic shower parametrization, taking as the jet response the superposition of the different single particle responses.

The jet energy resolution is evaluated here for two different geometric configurations: A) the Axial Field Spectrometer set-up (Fig. 2) with a box-like calorimeter 4λ deep and covering $\sim$ 2 units of rapidity, and B) a calorimeter infinitely deep and covering 4π. Two different calorimeter types were simulated: the AFS uranium calorimeter with $\sigma_e/(E) = 0.16E^{-1/2}$ for e.m. showers, $\sigma_h/(E) = 0.37\ E^{-1/2}$ and e/h = 1.11 for hadronic showers, and a non-compensated device with $\sigma_e/(E) = 0.16\ E^{-1/2}$, $\sigma_h(E)/E = 0.48\ E^{-1/2}$ and e/h = 1.48. For the AFS geometry, the results are given in Fig. 25a for single jets with Feynman-Field fragmentation [21], with the jet direction pointing to the centre of a calorimeter wall. At low energies, the jet resolution is seen to be dominated by the fluctuation of energy carried by particles outside the acceptance of the calorimeter ('geometry' fluctuations) and the fluctuations in 'available energy' due to fluctuations in the fragmentation process. In Fig. 26, the performance obtainable with a 4π geometry is shown for the two different types of calorimeters. The difference is particularly striking for large jet energies, $E_{jet} > 100$ GeV, where the resolution is dominated by the value of e/h. This is due to the fact that a large fraction of the jet energy is carried by a small number of particles, and a fluctuation of their composition (charged compared with neutral pions) gives a fluctuation in the calorimeter response. The size of this effect is to some degree dependent on the fragmentation scheme of the jet and a softer fragmentation may somewhat improve the resolution at the highest jet energies. The

resolution may also be improved by segmenting the calorimeter longitudinally so that the electromagnetic energy may be estimated separately. Other effects, such as the influence of the jet finding algorithm or the influence of soft particle background, should also be considered for a more complete evaluation of calorimeters for jet analysis [22].

7. OPERATIONAL EXPERIENCE AT THE ISR

The construction and installation of the 128 calorimeter modules in the ISR was phased over a 15 month period beginning with the installation of the 32 'roof' stacks (Fig. 2) in early 1981. The 2π calorimeter configuration was operated during approximately 5000 hours of colliding beam time in 1982 and 1983. The greatest fraction of this time was devoted to studies of pp collisions at a typical luminosity of $L \sim 10^{31}$ cm^{-2} s^{-1}; approximately 400 hours were devoted to $p\bar{p}$-running, with a luminosity close to 10^{29} cm^{-2} s^{-1} (using the superconducting low-ß insertion), and another 200 hours were devoted to $\alpha\alpha$, αp and dd collisions. For a very brief period, limited in time by the increase of background in the other intersections, pp data were taken with a luminosity of 1.4×10^{32} cm^{-2} s^{-1}, again using the superconducting low-ß insertion.

7.1 Electronics

A computerized high voltage system (manufactured by Danfysik, Roskilde, Denmark) provided the HV to the 3200 PMs. The HV settings could be set by computer in steps of 2 V and checked by reading the analogue voltages back in a scanning ADC. Apart from the individual settings, there was a provision to lower the HV on all tubes to a constant level (500 V) during the short periods of 'unstable beam' to protect the PMs from very large light levels. These interruptions occurred on average every 5-6 h and lasted for only a few minutes; stable calorimeter operation could be resumed within 5 min. after such an interruption.

We used LeCroy 2282B charge-integrating ADCs, which accept a 10 µ gate length necessary for the gain calibration using uranium noise. For data taking, the gate width was 130 ns, while for the absolute charge calibration a gate length of 1.2 µs was used. Apart from the linearity

requirements of better than 1% over the range of the ADCs (full scale was set to 40 GeV per tube in the hadronic section of a tower and to 10 GeV per tube in the e.m. section), we had a particularly severe requirement on the stability of the pedestal. In particular, systematic shifts of all pedestals--caused for instance by ambiant temperature fluctuations--had to be monitored at the level of 0.1 ADC count. Larger variations would have affected the energy scale of the calorimeter to an unacceptable level, particularly for events for which the energy deposit was distributed over a large fraction of the calorimeter acceptance. Typically, coherent 24 hour pedestal variations could be limited to $\leq$ 0.5 ADC counts; these variations were tracked and determined to $\sim$ 0.05 ADC counts by recording $\sim$ 5% of the events triggered at random intervals by a pulse generator rather than a particle interaction.

7.2 On-line energy monitoring

As explained in Section 4, the uranium radioactivity provided a stable 'light source', which allowed a sensitive monitoring of the complete optical readout chain. At the start of each ISR run, separated from the end of the previous one by typically 15 hrs, the PMs were allowed approximately 30 min to reach stable operation. At the end of the stabilizing period the gains of the PMs were determined using the uranium noise calibration, and voltage changes were calculated to reach the nominal gain settings. The computer also provided a condensed fault analysis of suspect PMs, which required operator intervention (disabling a channel etc.). An improved gain determination was made with the new HV settings, and this process was repeated until the actual and nominal gains agreed to within 1% (typically, 3-4 such iterations were sufficient for > 95% of the PMs). In general, the system was sufficiently stable for this calibration procedure to be repeated only once every 24 h.

Particular care was exercised to diagnose faulty PM channels in a semi-automatic way. Channels usually generate abnormally high signals (sparking of a faulty base, faults in the HV channels, etc.) In this experiment, where the trigger conditions predominantly involved information on transverse energy deposit of varied spatial topology, the trigger rates were very sensitive to the threshold settings. Malfunctioning readout channels could easily cause trigger rates much above the true physics

ones. A number of on-line monitoring tasks were developed, designed to detect incipient malfunctioning and to provide enough diagnostics to quickly solve the problems.

We note that our calorimeter was designed with a minimum of read-out redundancy, apart from the right-left pairing of PMs. A loss of a readout channel was hence a relatively serious fault, affecting the energy determination over a considerable area, because of the shower sharing of several towers. Care was therefore taken to limit the number of malfunctioning channels. Typically the calorimeter was operated with less than 20 inoperative channels out of 3200.

7.3 Triggering

The AFS physics programme concentrated on studies of hard scattering of nucleon constituents, which occur with cross-sections in the microbarn to picobarn range, in the environment of very high interaction rates. These studies had to await the availability of hadron calorimeters with excellent energy and space resolution and with powerful trigger capabilities. In the AFS we exploited both the momentum information obtained from on-line reconstruction of tracks in the drift chamber [23] and the topology of the energy deposition in the calorimeter [6].

The AFS employed a trigger processor with the capability of operating many triggers in parallel. Triggers which were based solely on information from the calorimeter operated on a two-level system, whereas four-level triggering was used for decisions which need additional information from the drift chamber.

The first level, or pretrigger, required a minimum number (usually 2) of hits in a barrel hodoscope surrounding the interaction region and a minimum energy deposit in the entire calorimeter (it was possible in the trigger software to restrict this energy sum to only the e.m. section of the calorimeter). The pretrigger caused all information from the event to be stored in the various data-acquisition modules, and initiated the second-level trigger, which was carried out in a special-purpose digital processor called the Very Fast Bus (VFB).

The VFB was a trigger processor based on look-up table procedures, capable of analysing in parallel many trigger conditions. The event information was encoded on 50 data lines, with the analog signals from the calorimeter encoded on 26 lines. The remainder of the input data were logic signals derived from information in particle detectors other than the calorimeter. The 50 encoded lines were grouped in five blocks of ten lines, which served to address 51 separate blocks of 1024 X 1 bit random access memories. Each trigger 'decision' consisted of five memory blocks which were addressed by the five groups of encoded lines: for a valid trigger, all five of the memory locations addressed by the input data must be set to '1'. Triggers were therefore defined by the contents of the memories and were controlled by the trigger software.

The system operated completely in parallel, so that any number of the 51 possible triggers could be simultaneously in operation. The processing time for the VFB was 400 ns, independent of the event configuration or number of triggers selected.

The input data to the analog signal processor for the calorimeter were signals from the PM dynode outputs, summed over the rapidity range of a group of 16 calorimeter towers at constant azimuth. There are 52 total energy dynode sums, and 48 dynode sums of the e.m. sections only. Each of these sums, represented as one block in the inner square of Figure 27, was passed through a double delay line shaping amplifier with a clipping time of 60 ns. The total energy signal, which was used in forming the pre-trigger, was obtained by adding the outputs of the 52 shaped dynode energy sums. A total of 48 'single particle' sums were formed by adding two neighbouring total energy dynode sums, except at the corners of the calorimeter, where the copper calorimeter sums were also included. The 24 'jet' sums were formed by adding three single particle sums, thus summing total energy from six contiguous total energy dynode sums. To avoid edge effects, both the single particle sums and the jet sums overlapped, as shown in Fig. 27. Altogether, 122 sums were sent to multilevel discriminators (Table 4). For each level of discrimination, the number of distinct groups of non-zero discriminators was counted by the processor, and the results encoded into two bits (0, 1, 2, $\geq$ 3 discriminators) which are input data for the VFB. For the e.m. signals, the corresponding single

particle sums were required to fall within an energy window before they contributed to the multiplicity count. For the total energy and electromagnetic energy sums, the highest non-zero discriminator level was encoded onto three data lines for the VFB.

For triggers involving the drift chamber (e.g. the electron trigger), a four-level trigger system was used. In this case drift-chamber information was used to determine if a track with momentum above a given threshold was in coincidence with e.m. energy above some threshold in a calorimeter tower at the same azimuth as the track. The first and second levels were processed in the same way as the normal calorimeter triggers, the VFB decision requiring a localized energy deposit in the electromagnetic part of the calorimeter. The third level demanded that a minimum number of drift-chamber signals be in geometrical correspondence with the calorimeter tower. This level required 1.5 μs to reach its decision. In the fourth level, a microprocessor (ESOP) read the time-digitized drift chamber signals and reconstructed the tracks (in the azimuthal plane only) to make the final decision [23]. The time required by the fourth level depended on the event configuration; typically it was less than 1 ms.

Table 4

Trigger possibilities of the analog trigger processor

Sum	No. of sums	No. of calor. rows (summed at const. azimuth)	No. of discriminator levels
Total energy	1	48 + 4	5
Total e.m. energy	1	48	4
e.m. single particle	48	1	3
Hadronic single particle	48	2	4
Jet	24	6	3

7.4 Pattern reconstruction

The AFS calorimeter pattern reconstruction program aims at identifying local energy clusters, corresponding as much as possible to showers produced by single particles. The clustering is performed solely on the basis of the calorimeter information and completely decoupled from the tracking information provided by the central drift-chamber detector. Matching of reconstructed charged tracks with calorimeter energy clusters or merging of clusters in regions of high particle density (e.g. inside jets) can be made at a later stage of the analysis.

In the initial pass, energy clusters in nine towers are formed around peak towers with energy above a given threshold (chosen as 2.5 σ above the pedestal). The 3 x 3 cluster size is justified by the results of the beam tests (see Section 5.5 and Fig. 22). Adjoining towers in the same stack are added to the cluster if their energy is consistent with light-sharing from a single shower within the stack. These considerations apply separately to the electromagnetic and hadronic sections: for a low-energy e.m. cluster for example, only the electromagnetic energy might be retained. Most final clusters, however, consist of energy from both electromagnetic and hadronic sections. Towers may belong to more than one cluster; in this case an energy-sharing algorithm uses the surrounding energy deposition to distribute the tower energy between the two clusters. Subsequently, energy clusters are examined for their consistency with the single shower hypothesis, and decisions are made to split or to merge clusters accordingly. The pattern recognition is performed on each of the four calorimeter walls in turn, with the copper stacks incorporated as an additional hadronic row in each adjacent wall.

The energies and positions of the final clusters are computed as weighted sums over the towers in the cluster, the weights being determined from the test-beam measurements. The observed linearity of the calorimeter response to electrons with energies up to 10 GeV (see Fig. 13) led to the adoption of the electron energy scale for all clusters. Corrections for non-e.m. energy can be later determined using the Monte Carlo program (Section 6.1); these corrections are smaller than for a conventional calorimeter because of the approximate equality of response to electrons and hadrons.

Some care has to be taken to consider the effects of the radioactivity which gives rise to a number of apparent low-energy 'noise' clusters in each event. This effect can be studied by examining out-of-time events, for which only the noise from the radioactivity is registered.

The performance of the calorimeter pattern recognition is illustrated in Fig. 28. The position and energy of reconstructed calorimeter clusters are compared with those of charged tracks reconstructed in the drift chamber and extrapolated to the front face of the calorimeter. The results shown are for a sample of high p_T tracks ($\langle p_T \rangle \simeq 2.75$ GeV) with an angle of incidence varying between 0° and $\sim$ 45°. Position resolutions $\sigma_x \simeq 8$ cm and $\sigma_z \simeq 10$ cm were achieved, where x is the coordinate along the stack (i.e. in the light-sharing direction) and z is the coordinate across the stack. The dashed curve in Fig. 28c shows the expected energy distribution computed from the test-beam results convoluted with the incident charged-particle p_T spectrum. Similar results have been obtained at lower p_T (p_T = 300-1000 MeV) using isolated charged particles in minimum-bias data.

The spatial resolution is not as good as would have been expected from the test-beam results. Most likely, we see here the effect of the overlap with other (low-energy) clusters. Note, however, that the energy resolution, as measured in Fig. 28c corresponds to $\sigma/E \sim 0.35/\sqrt{E}$ (GeV), consistent with the test-beam results.

An example of a two-jet event is shown in Fig. 29. The high granularity of the tower construction and the good energy resolution make off-line results closely ressemble the raw on-line information.

7.5 Operation at $L = 1.4 \times 10^{32}$ cm^{-2} s^{-1}

For a short period in December 1982 the ISR was operated at a luminosity of $L = 1.4 \times 10^{32}$ cm^{-2} s^{-1} at $\sqrt{s} = 53$ GeV, corresponding to a mean time between inelastic collisions of about 200 ns. Data were taken in the AFS under a variety of trigger conditions and compared with data taken at the same energy but at a luminosity of $L = 3 \times 10^{30}$ cm^{-2} s^{-1}.

In this run we aimed at exploring the rate limitations of the spectrometer in view of a possible measurement of jet production close to the kinematical limit [$x_T \sim 1$] and which required the highest possible interaction rates [24]. Apart from technical difficulties associated with high-rate operation of drift chambers and calorimeters, care must be exercised to recognize 'pile up' effects. Trigger conditions may preferentially be satisfied through accidental overlap of two or more events within the sensitive detector time chosen to produce the trigger condition. In Table 5 we summarize the effect of pile-up on trigger rates for three different trigger geometries: a very non-selective trigger on total energy deposit, particularly sensitive to pile-up, a moderately restrictive trigger on 'jets', and a rather restrictive trigger on pairs of high p_T e.m. particles, not likely to be satisfied by two separate events.

Table 5
Trigger sensitivity to interaction rate

Trigger	$\frac{\text{Trigger rate at } L_{High}/L_{High}}{\text{Trigger rate at } L_{Low}/L_{Low}}$
Total energy ($E_T > 28$ GeV)	4
Jet ($E_T > 9$ GeV in ~ 1 sr	1.5
Two e.m. single particles (each calorimeter row with $E_{em} > 4$ GeV)	1.0

The tolerable level of pile-up will depend on the details of the event structure and on the physics analysis of the recorded collisions. As an example, for the "total-energy" triggered events, pile-up cannot be tolerated and one would have to ensure that pile-up events are rejected with 100% efficiency or that the collision rate is low enough that unrecognized pile-up events do not effect the physics conclusions. In the former case a simple calculation shows that the optimum luminosity is given by $L_{opt} = 1/2\sigma_{eff} \cdot \delta$, where σ_{eff} is the total cross section to which the experiment is sensitive ($\sim$ 30 mb in our case) and δ is the integration time of the detector (δ = 130 ns for our calorimeter) and where we required that a collision of interest is not preceded or followed by another collision within δ seconds. Under such conditions one finds for the optimum luminosity $L_{opt} \simeq 10^{32}$ cm^{-2}s^{-1}. In reality, our

pile-up rejection was not perfect and we estimate that approximately 90% of the pile-up events could be recognized and rejected. Consequently, the acceptable luminosity for the study of "total-energy" triggered events is closer to $L \simeq 10^{31} cm^{-2} s^{-1}$. A very different result is obtained for events recorded with the "jet" or "e.m. single particle" trigger. Additional events within the sensitive time of the detector rarely help satisfy the trigger condition (see Table 5) and influence the physics analysis to a much lesser extend. We estimate that for these more restrictive trigger and analysis conditions the optimum luminosity is closer to $L_{opt} \simeq 5 \times 10^{32} cm^{-2} s^{-1}$.

An identical analysis was carried out on jet-triggered data recorded at the two different luminosities to assess both the performance of the detectors and the reconstruction programs.

7.5.1 Performance of the drift chamber

In contrast to normal operation, high-luminosity running required some layers to be operated at lower gas gains to keep the operating currents below a safe limit (gain reduction up to a factor of 5 in the inner layers, but no gain reduction in the outer ones). Care was taken not to vary the drift field, and we measured no change in drift velocity (v_D = 52 mm/μs). With the standard calibration and reconstruction programmes a change in resolution from $\sigma \sim 220$ μm (normal luminosity) to $\sigma \sim 320$ μm (high luminosity) was observed. On average, 15.7 tracks (reconstructed average track length = 30.1 cm) were associated with an event taken at high luminosity, compared to 14.4 tracks (average reconstructed track length, 37.6 cm) in the low-L sample. CPU time/event was found to be approximately proportional to the total number of tracks (in-time and out-of-time), and was approximately twice as long compared to the analysis time at 'standard' luminosity of $< \simeq 2 \times 10^{31} cm^{-2} s^{-1}$.

7.5.2 Calorimeter performance

The two data samples were analysed with the standard programs for the cluster reconstruction and a jet-finding algorithm. The p_T spectra of the jets are shown in Fig. 30. These are raw data, not corrected for trigger threshold effects, which are clearly visible at low p_T. Over most of the p_T range the two spectra agree rather well, with the low-L data showing an excess at high values of p_T. These events are cosmic-ray

background events in coincidence with a pp interaction, which are obviously more pronounced in the low-L sample. With more refined diagnostics--4 ns event timing on the calorimeter and an energy deposit history in 10 ns bins, in thirty-two 10 ns time bins (installed only after this run and hence not available for these data)--a further improvement could certainly be obtained. These results show that calorimeters can be operated and used for physics analysis at luminosities in excess of 10^{32} cm^{-2} s^{-1}. The precise luminosity limits depend not only on the time characteristics of the instrument but to a larger extent on the selectivity of the trigger and on the topology of the energy deposit of interest relative to the 'average' inelastic collision [22].

8. CONCLUSION

We have discussed the construction, performance, and operation of a uranium/scintillator sampling calorimeter. Essential to the success of the programme were the following features:

- Excellent energy resolution and nearly identical response to e.m. and hadronic showers permitted to record and analyse a great variety of reactions with a minimum of off-line corrections.

- A dedicated trigger system, using analog computation, matched the versatility of the instrument. Parallel data acquisition of diverse physics topics maximized the use of the ISR beam time.

- The tower structure was essential in the pattern reconstruction and for extracting physics in the off-line analysis. The rectangular geometry of the modules both minimized the effects of cracks where energy could be lost and of particles giving abnormal response in the WLS system. It reduced, however, the effective granularity below the geometrical one for non-normally incident particles and somewhat complicated the pattern reconstruction.

- The scintillator readout system proved to be well matched to the detection requirements at the ISR. We remarked on the limitations of such methods, at higher energies, where control of instrumental effects

at the one-per-cent level is required. Radiation damage to scintillators and WLS may further restrict the range of applications. The uranium radioactivity signal was a bonus for achieving reliable operation, but introduced low-energy noise and required additional care at the pattern-reconstruction level.

ACKNOWLEDGEMENTS

The uranium calorimeter project would have been impossible without the continuous and courageous support of many people. D. Berley and W. Wallenmeyer were instrumental in the procurement of the Uranium. P. Falk-Vairant, then Director of Research at CERN, unfailingly encouraged us to persist, as did Sir John Adams, E. Gabathuler, and I. Mannelli. We are sincerely grateful to A. Minten, then Leader of EF Division, under whose responsibility the uranium calorimeter was built.

We acknowledge with pleasure and gratitude the outstanding technical assistance we received from many people, in particular from D. Guyon, H. Hofmann, G. Kantardjian, A. Lefèvre and C. Marin.

REFERENCES

[1] H. Gordon et al., Nucl. Instrum. Methods 196 (1982) 303.
O. Botner et al., Nucl. Instrum. Methods 196 (1982) 314.

[2] T. Akesson et al., Phys. Lett. 118B (1982) 185.

[3] C.W. Fabjan and T. Ludlam, Ann. Rev. Nucl. Part. Sci. 32 (1982) 335.

[4] O. Botner, Phys. Scripta 23 (1981) 555;
O. Botner et al., Nucl. Instrum. Methods 179 (1981) 45.

[5] C.W. Fabjan et al., Nucl. Instrum. Methods 141 (1977) 61.

[6] C.W. Fabjan, Proc. Int. Conf. on High Energy Physics, Madison, p.867; L. Durand and L.G. Pondrom (1980), Ed.
L. Rosselet, Proc. Topical Conf. on the Application of Microprocessors to High-Energy Physics Experiments p.316, CERN 81-07 (1981).

[7] J.W.Tuyn; Recommendations for the safe use of uranium at CERN, CERN TIS Safety Note No.7 (1979).

[8] R.L. Garwin, Rev. Sci. Instrum. 31 (1960) 1010;
W.B. Atwood et al., SLAC-TM-76-7 (1976);
V. Eckardt et al., Nucl. Instrum. Methods 155 (1978) 389;
W. Selove et al., Nucl. Instrum. Methods 161 (1979) 233.

[9] W. Kienzle, CERN-NP Int. Rep. 75-12, (1975).

[10] H. Schönbacher and W. Witzeling, Nucl. Instrum. Methods 165 (1979) 517.

[11] Y. Sirois and R. Wigmans, CERN-EP/85-60, submitted to Nucl. Instrum. Methods.

[12] R.W. Sternheimer et al., Phys. Rev. B3 (1971) 3681;
S. Seltzer and M. Berger, NAS-NRC, Publication 1133, p. 187.

[13] R.L. Ford and W.R. Nelson, SLAC report 210 (1978).

[14] T.A. Gabriel, Nucl. Instrum. Methods 150 (1978) 145.

[15] A. Grant, Nucl. Instrum. Methods 131 (1975) 167.

[16] Y. Oren, Internal AFS Note 161 (1980), unpublished.

[17] R.K. Böck et al., Nucl. Instrum. Methods 188 (1982) 507.
O. Benary, Internal AFS Note 313 (1981), unpublished.

[18] T. Akesson et al., Phys. Lett. 123B (1983) 133.

[19] T. Akesson et al., Phys. Lett. 128B (1983) 354.

[20] T. Akesson et al., Z. Phys. C25 (1984) 13.

[21] R.D. Field and R.P. Feynman, Nucl. Phys. B136 (1978) 1.

[22] T. Akesson et al., Jets at the Large Hadron Collider, Proc. CERN-ECFA Workshop on the Feasibility of Hadron Colliders in the LEP Tunnel, Lausanne and Geneva, 1984 (Report ECFA 84/85 and CERN 84/10, Geneva, 1984, p.167).

[23] S. Cairanti et al., The microprogrammable processor ESOP in the AFS trigger system, Proc. Topical Conf. on the Application of Microprocessors to High-Energy Physics Experiments, Geneva 1981 (CERN 81-07, Geneva (1981), p.321.

[24] The Axial Field Spectrometer Collaboration, 'Physics at the limit of phase space'; Proposal CERN/ISRC/82-17 (1982).

FIGURE CAPTIONS

Fig. 1 Cross-section through the Axial Field Spectrometer. The beam pipe is surrounded by a cylindrical hodoscope, followed by a tracking chamber with highly redundant 'imaging' readout. The hadron calorimeter covers the complete azimuth in four similarly arranged 'walls' of uranium/scintillator units. The vertical and the lower horizontal walls could be retracted for access to the central drift chamber.

Fig. 2 Isometric view of the AFS calorimeter, surrounding the central tracking detector in four 'walls'.

Fig. 3 Horizontal cross-section and vertical side view of a calorimeter unit showing the support of the absorber and scintillator plates, the layout of the light guides and the PM mounts.

Fig. 4 Isometric view of one of the 128 'stacks'. The enlargement shows the readout of the e.m. front section.

Fig. 5 Light yield of acrylic scintillator (PMMA) relative to NE 102A as a function of naphthalene content in PMMA (1% butyl-PBD, no secondary scintillating agent), measured via a BBQ-doped wavelength shifter.

Fig. 6 Transmission curve for BBQ. Emission spectra for butyl-PBD, POPOP, and BBQ.

Fig. 7 Absorption length as a function of wavelength for acrylic doped with UVA or BBQ.

Fig. 8 Uniformity of response across a calorimeter cell for two different WLS plates (3 mm thick, UV transparent; 2 mm thick, UV absorbing). The measurement was performed with a collimated ruthenium source on a prototype of different width (300 mm) compared to that of the final detector.

Fig. 9 Attenuation of light along the wavelength shifter for the e.m. and hadronic sections.

Fig. 10 a) Calculated reduced energy resolution [$\sigma(E)/\sqrt{E}$] for electrons as a function of electron energy and attenuation of the scintillator. A calorimeter with an intrinsic resolution $\sigma(E)/\sqrt{E} = 0.16$ was assumed. The energy resolution for electrons is deteriorated due to the light attenuation, when the response is averaged over the cross-section of a calorimeter tower. For example, a 100 GeV electron registered with scintillator of $\lambda = 15.2$ cm would be observed with an effective resolution of $\sigma(E)/\sqrt{E} \simeq 0.8$ instead with the intrinsic resolution of $\sigma(E)/\sqrt{E} = 0.16$.
b) As in (a) but for hadrons, for which a resolution of $\sigma(E)/\sqrt{E} = 0.37$ was assumed.
See text for comments on radiation damage.

Fig. 11 a) As in Fig. 10, but showing the influence of the attenuation in the WLS assumed to follow an exponential law, which in reality is not strictly correct. Electrons with an intrinsic resolution of $\sigma(E)/\sqrt{E} = 0.16$ were assumed;
b) As a) but for hadrons, measured with an intrinsic resolution of $\sigma(E)/\sqrt{E} = 0.37$.

Fig. 12 Measured calorimeter response for 4 GeV/c pions. The arrows indicate the range of the distribution to which a Gaussian fit was made for the determination of the resolution.

Fig. 13 Linearity of calorimeter response and calorimeter resolution [$\sigma(E)/\sqrt{E}$] for electrons with momenta in the range 1.0 to 10 GeV.

Fig. 14 Linearity and resolution [$\sigma(E)/\sqrt{E}$] of the calorimeter for hadrons with momenta in the range 4-40 GeV/c.

Fig. 15 Calorimeter response to π^+, π^-, and protons in the momentum range 0.2 to 4.0 GeV/c. The response is identical within errors for the three particles, provided the 'available' energy is considered (equal to kinetic energy for protons, to total energy for pions). The extent of the vertical bars on the measured points cover the range between $+1\sigma$ and -1σ of the measured resolution.

Fig. 16 Measured energy deposit for 4 GeV/c electrons and hadrons as a function of the calorimeter gate length. The results are normalized to the value at 120 ns gate length.

Fig. 17 Energy resolution for pions (left ordinate) and electrons (right ordinate) versus gate length at 4 GeV/c.

Fig. 18 The ratio of electron to hadron response in the 400 to 4000 MeV available energy range. The solid line represents a Monte Carlo calculation of the response, assuming that the particle looses energy by ionization only up to the interaction point; for the remaining energy the asymptotic hadronic response with e/h = 1.11 is assumed.

Fig. 19 The ratio of e.m. to hadronic energy response as a function of energy for different calorimeter systems.
(38% Cu, 67% U. scint., this publication; U/LAr Ref. [5]; Cu/scint. Ref. [4]; Fe/LAr: Ref. [5]; Fe/Scint. (1) Abramowicz et al., Nucl. Instr. Methods 180, 429(1981);(2) A. Beer et al., Nucl. Instr. Methods 224 (1984), 360.

Fig. 20 Pion rejection measured in the calorimeter operated in the ISR-environment during data-taking for a fixed electron efficiency of 75%.

Fig. 21 Position resolution along the x (light sharing) direction of a stack, measured with normally incident 4 GeV/c electrons. The position is obtained by comparing the signal in adjacent towers, x [cm] = 10 · (U - D)/(U + D). The error bars represent the r.m.s. position accuracy ($\sigma \simeq$ 1cm). The position measurement and resolution is essentially independent of the y position of impact (0, Δ, +).

Fig. 22 Dependence of the energy response on the azimuthal angle of incidence, measured for 4 GeV/c pions. The angle ϕ gives the deviation from normal incidence. Shown are the sums over three and nine towers.
b) Reduced energy resolution, $\sigma(E)/\sqrt{E}$ versus azimuthal deviation ϕ from normal incidence. When the deposit in a 3 x 3 tower matrix is measured, the resolution is independent of the angle of incidence up to 45° with respect to normal incidence.

Fig. 23 Position resolution along the y (width) direction of a tower, measured with normally incident 4 GeV/c electrons. The position is obtained by comparing the signals in the left and right phototubes. The error bars represent the rms width of the resolution ($\sigma \simeq 1$ cm).

Fig. 24 The worst-case optical non-uniformity: scan with a 4 GeV/c electron beam, under normal incidence across the gap between neighbouring stacks. The approximately 15% non-uniformity can be further reduced with a correction algorithm using the two signals in each tower A and B (short-dashed curve, see text).

Fig. 25 a) Monte Carlo calculation of the jet resolution of the uranium calorimeter. At low energies the resolution is dominated by 'geometry' fluctuations (dashed line, leakage of jet energy out of the acceptance of the calorimeter) and by fluctuation of the available energy (dash-dotted line).
b) As in (a) but evaluated for a non-compensated calorimeter.

Fig. 26 Monte Carlo calculation of the jet resolution for an 'infinitely' thick, 4π calorimeter. The advantage of a (nearly) compensated calorimeter is particularly evident at very large jet energies. For uncompensate calorimeters, the resolution ceases to improve as $E^{-1/2}$ in the high-energy limit.

Fig. 27 Schematic diagram of the calorimeter trigger sums. The triangles represent the hadronic sums. Two adjacent hadronic sums are combined into the single particle sums, and the next level of summing corresponds to the jet sums. One should notice that the Cu-module hadronic sums are simply added to the single particle sums coming from the corners of the calorimeter.

Fig. 28 Position match between reconstructed tracks in the drift chamber and showers localized in the calorimeter:
a) in the direction along the stack: the position interpolation is based on light sharing between adjacent towers;
b) in the direction parallel to the beams;

c) Difference between the shower energy E in the calorimeter and the momentum measurement p in the drift chamber for particles with measured momentum $p > 2.75$ GeV/c and $E > 2$ GeV. The dashed line shows the distribution expected from the nominal calorimeter resolution of $\sigma(E)/E = 0.36/\sqrt{E}$ folded with the known p_T spectrum of charged particles.

Fig. 29 Energy deposition in the calorimeter towers from a two-jet event, showing the fine granularity of the calorimeter towers (a); the same event reconstructed with the calorimeter reconstruction program in bins of $\Delta\eta = 0.2$ and $\Delta\phi = 10°$. An energy deposit $E_{jet} > 8.5$ GeV in $\Delta\phi = 45°$ was required in the trigger.

Fig. 30 The p_T spectra of jets as measured in two ISR runs with low and very high luminosities. Over a substantial p_T interval the two spectra coincide within the (statistical) errors. At very large p_T, the high-luminosity sample is consistently below the low-luminosity one, the latter being more strongly contaminated by cosmic rays, which are not fully eliminated in this analysis. The two data samples have been normalized to the same integrated luminosity.

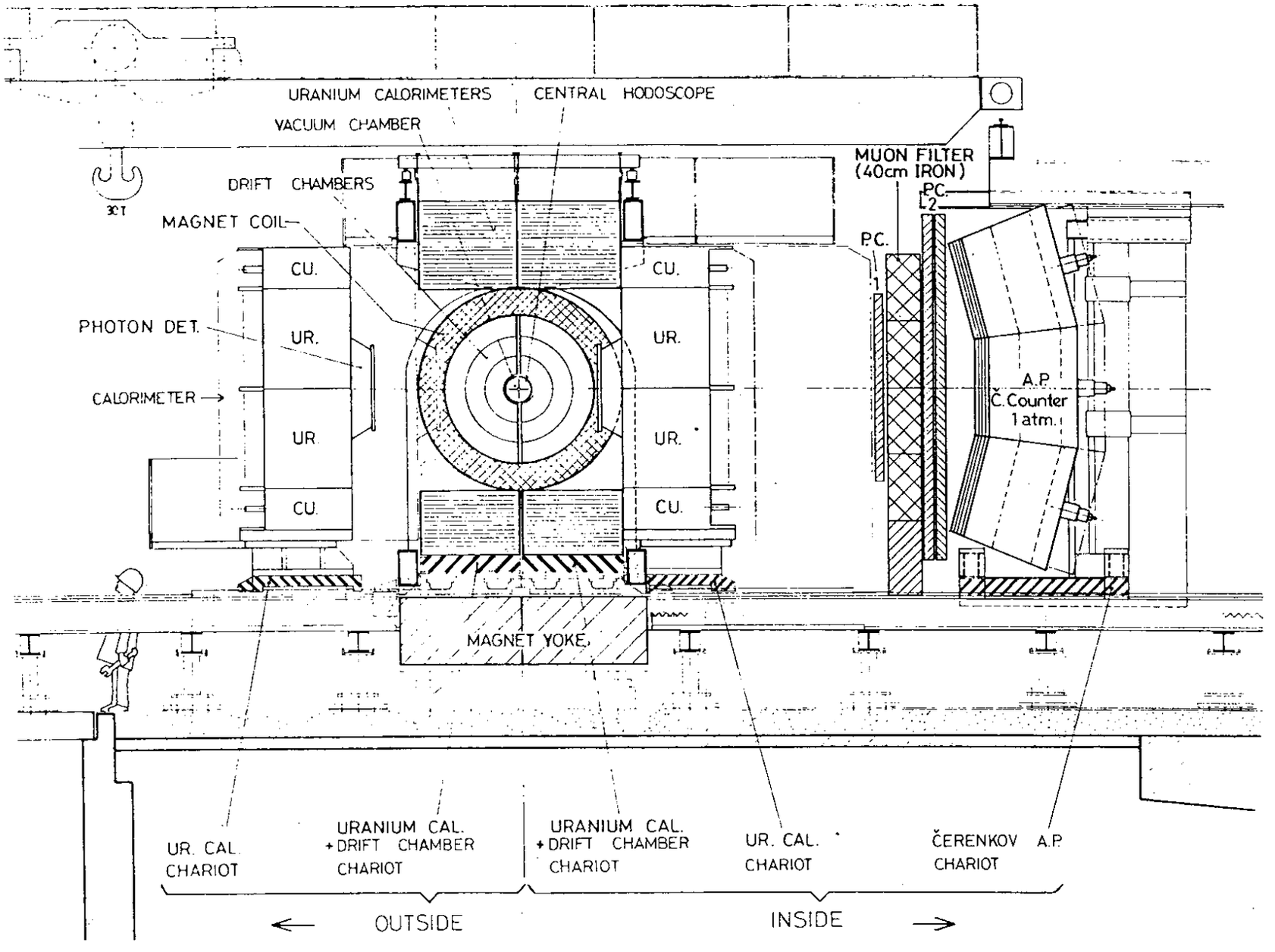
URANIUM CALORIMETERS
CENTRAL HODOSCOPE
VACUUM CHAMBER
MUON FILTER
(40cm IRON)
DRIFT CHAMBERS
30T
MAGNET COIL
P.C.
2
P.C.
1
CU.
UR.
PHOTON DET.
CALORIMETER
A.P.
Č. Counter
1 atm.
MAGNET YOKE
UR. CAL.
CHARIOT
URANIUM CAL.
+ DRIFT CHAMBER
CHARIOT
URANIUM CAL.
+ DRIFT CHAMBER
CHARIOT
UR. CAL.
CHARIOT
ČERENKOV A.P.
CHARIOT
OUTSIDE
INSIDE

Fig. 1

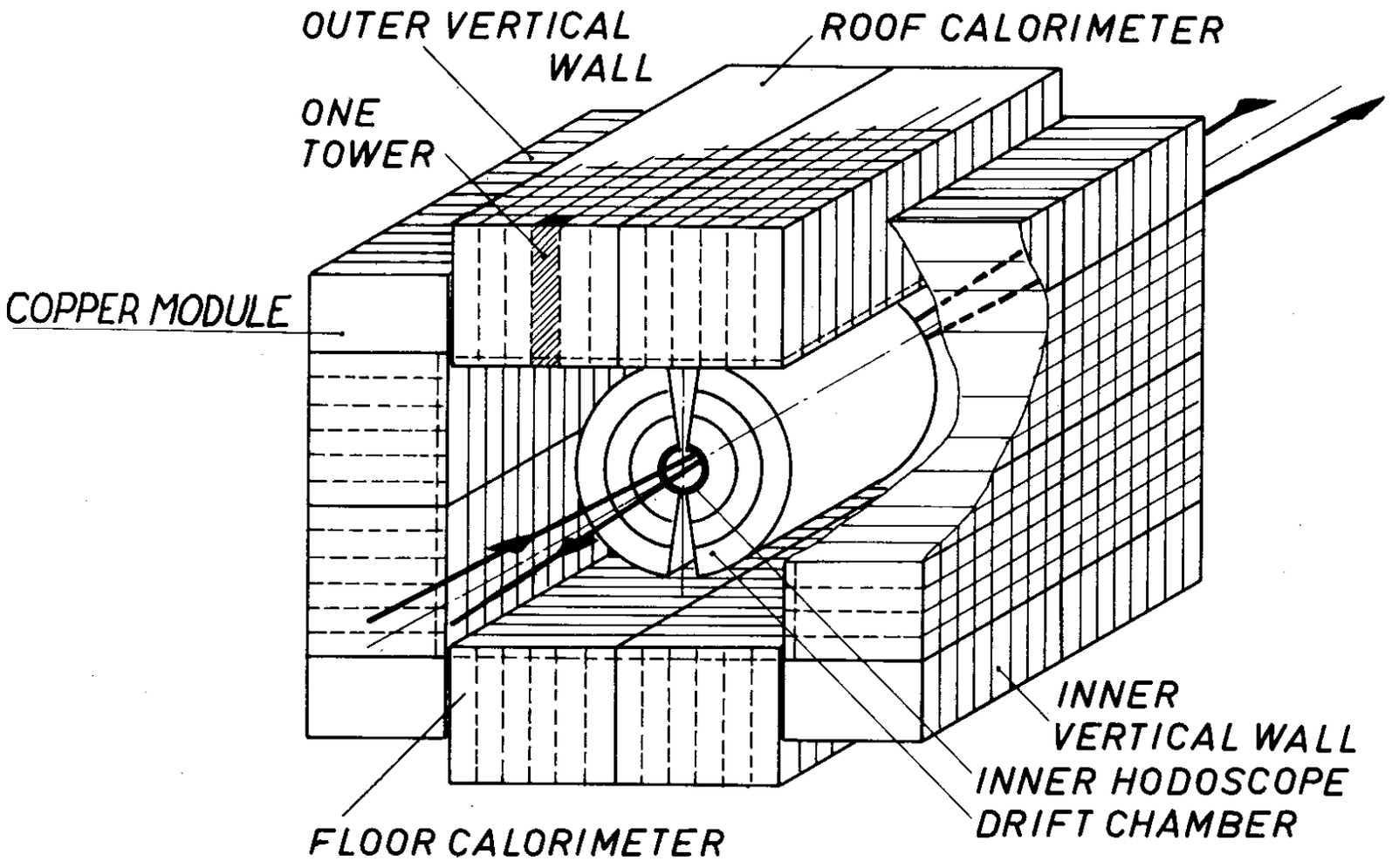
OUTER VERTICAL WALL
ROOF CALORIMETER
ONE TOWER
COPPER MODULE
INNER VERTICAL WALL
INNER HODOSCOPE
DRIFT CHAMBER
FLOOR CALORIMETER

Fig. 2

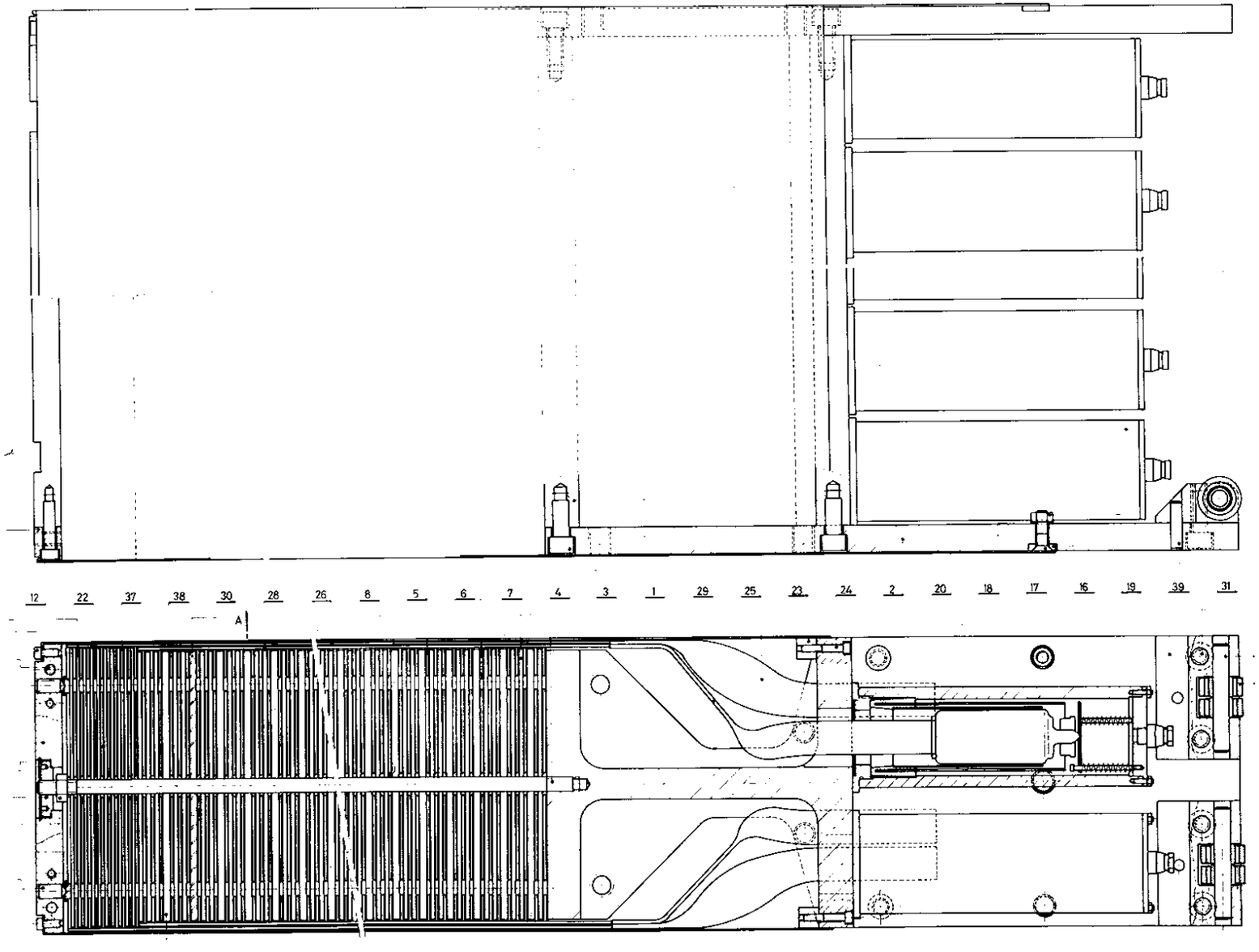

Fig. 3

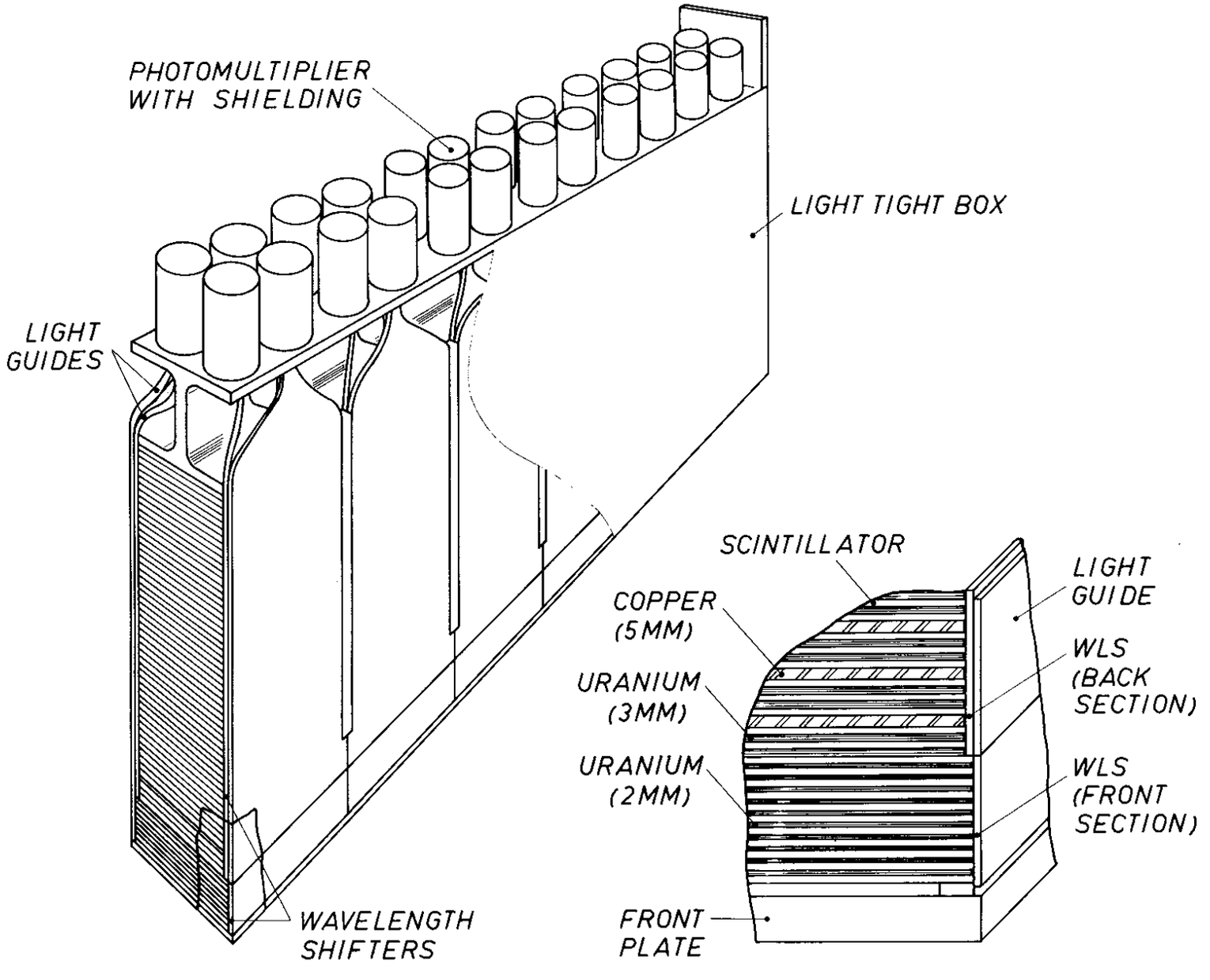
PHOTOMULTIPLIER
WITH SHIELDING
LIGHT TIGHT BOX
LIGHT
GUIDES
WAVELENGTH
SHIFTERS
SCINTILLATOR
LIGHT
GUIDE
COPPER
(5MM)
WLS
(BACK
SECTION)
URANIUM
(3MM)
URANIUM
(2MM)
WLS
(FRONT
SECTION)
FRONT
PLATE

Fig. 4

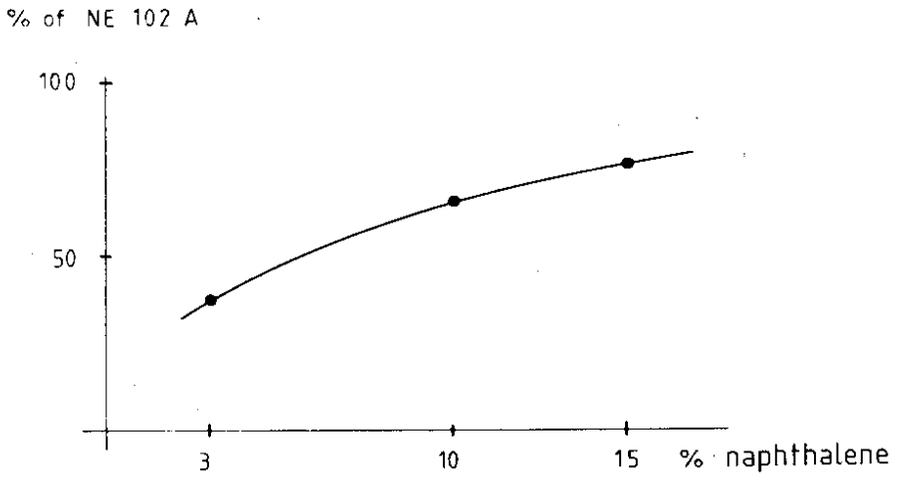
% of NE 102 A
100
50
3
10
15
% naphthalene

Fig. 5

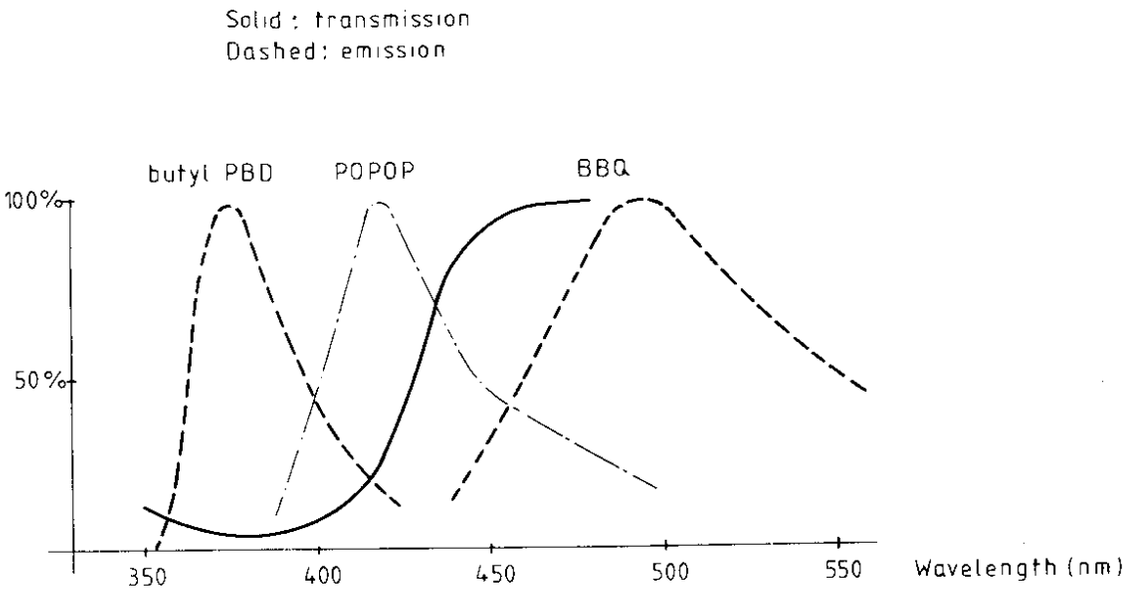
Solid : transmission
Dashed: emission
butyl PBD
POPOP
BBQ
100%
50%
350
400
450
500
550
Wavelength (nm)

Fig. 6

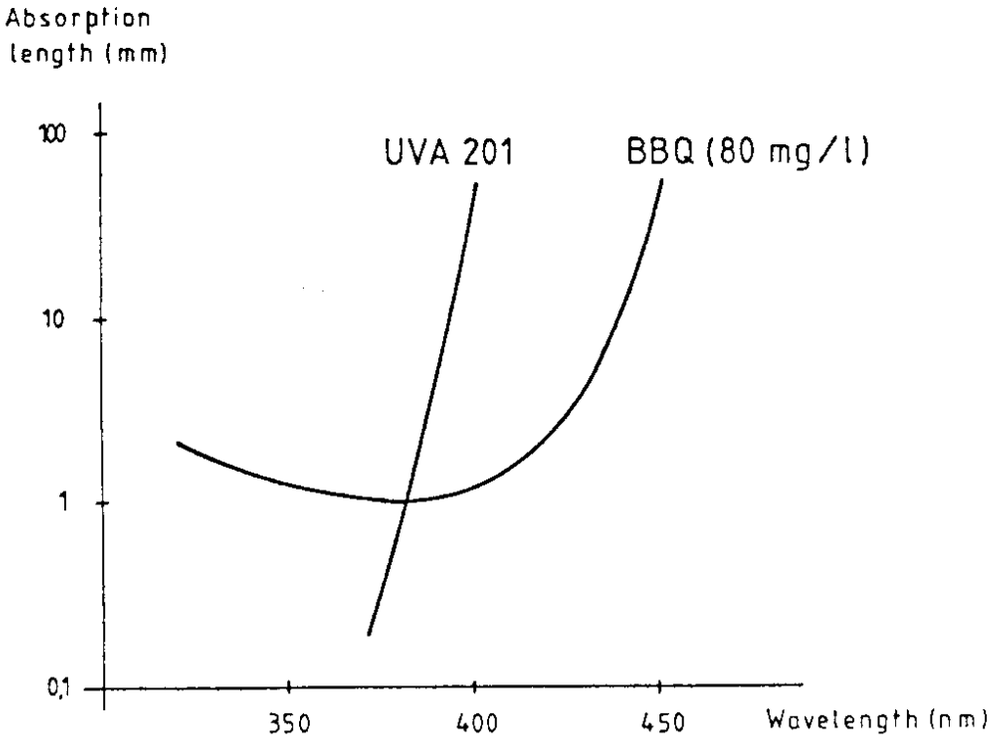
Absorption
length (mm)
100
10
1
0,1
UVA 201
BBQ (80 mg/l)
350
400
450
Wavelength (nm)

Fig. 7

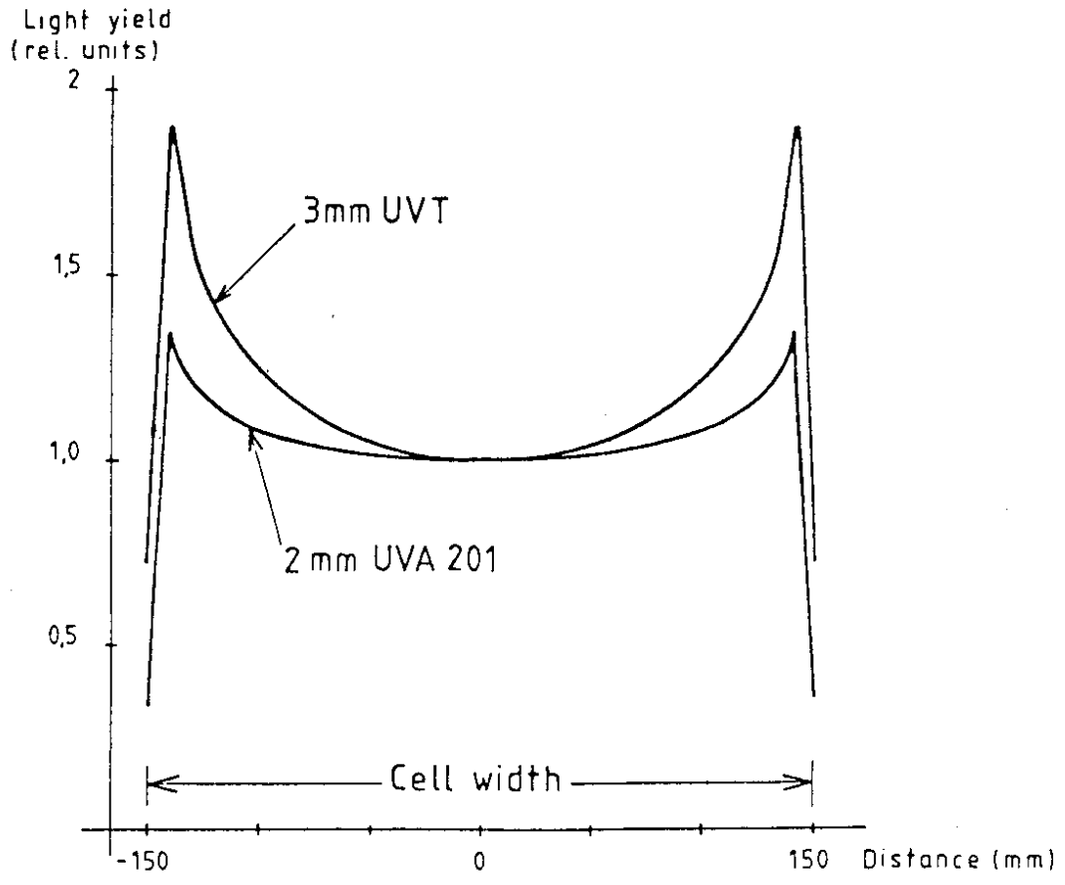
Light yield
(rel. units)
2
1,5
1,0
0,5
3mm UVT
2 mm UVA 201
Cell width
-150
0
150
Distance (mm)

Fig. 8

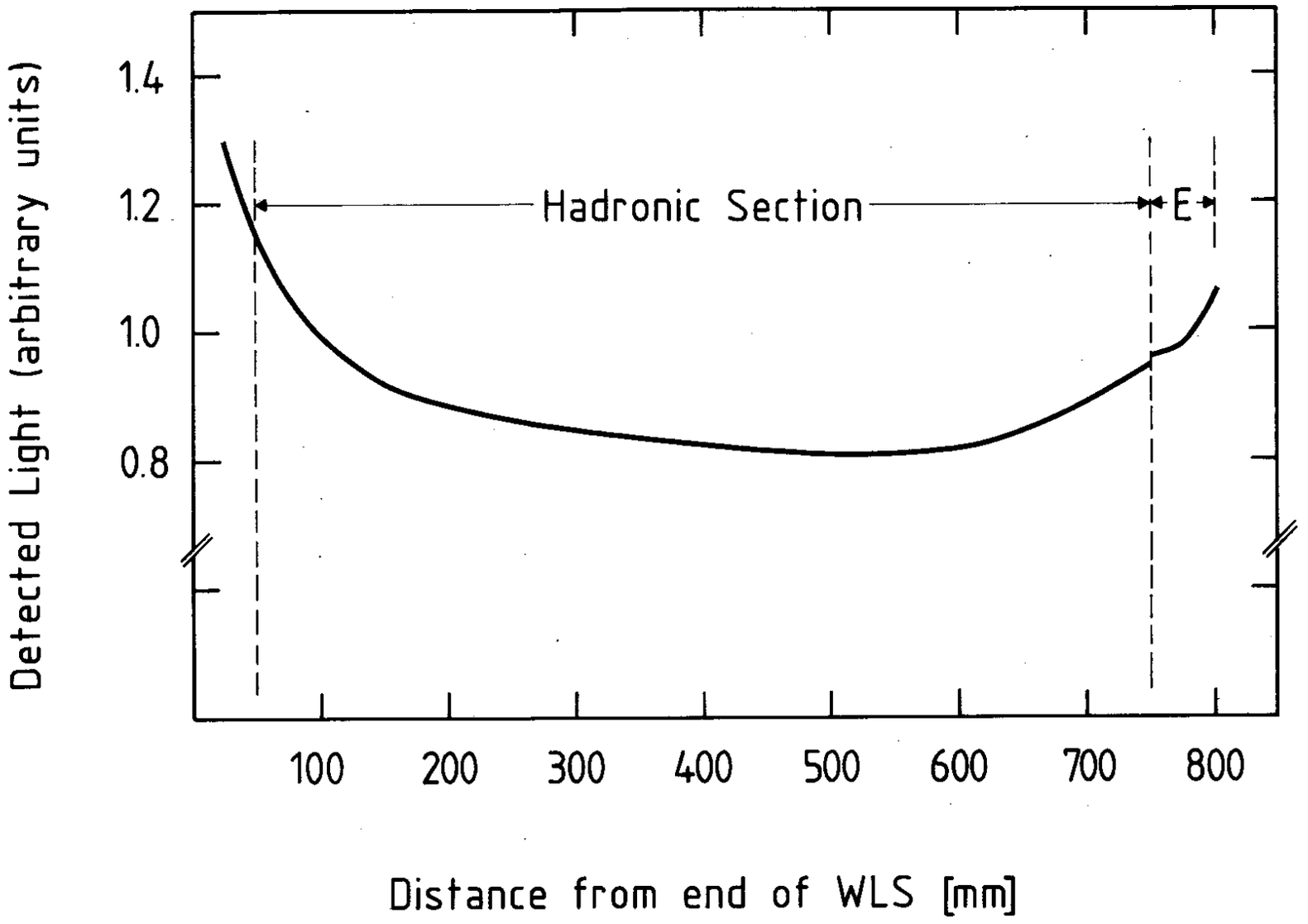
Detected Light (arbitrary units)
1.4
1.2
1.0
0.8
Hadronic Section
E
100
200
300
400
500
600
700
800
Distance from end of WLS [mm]

Fig. 9

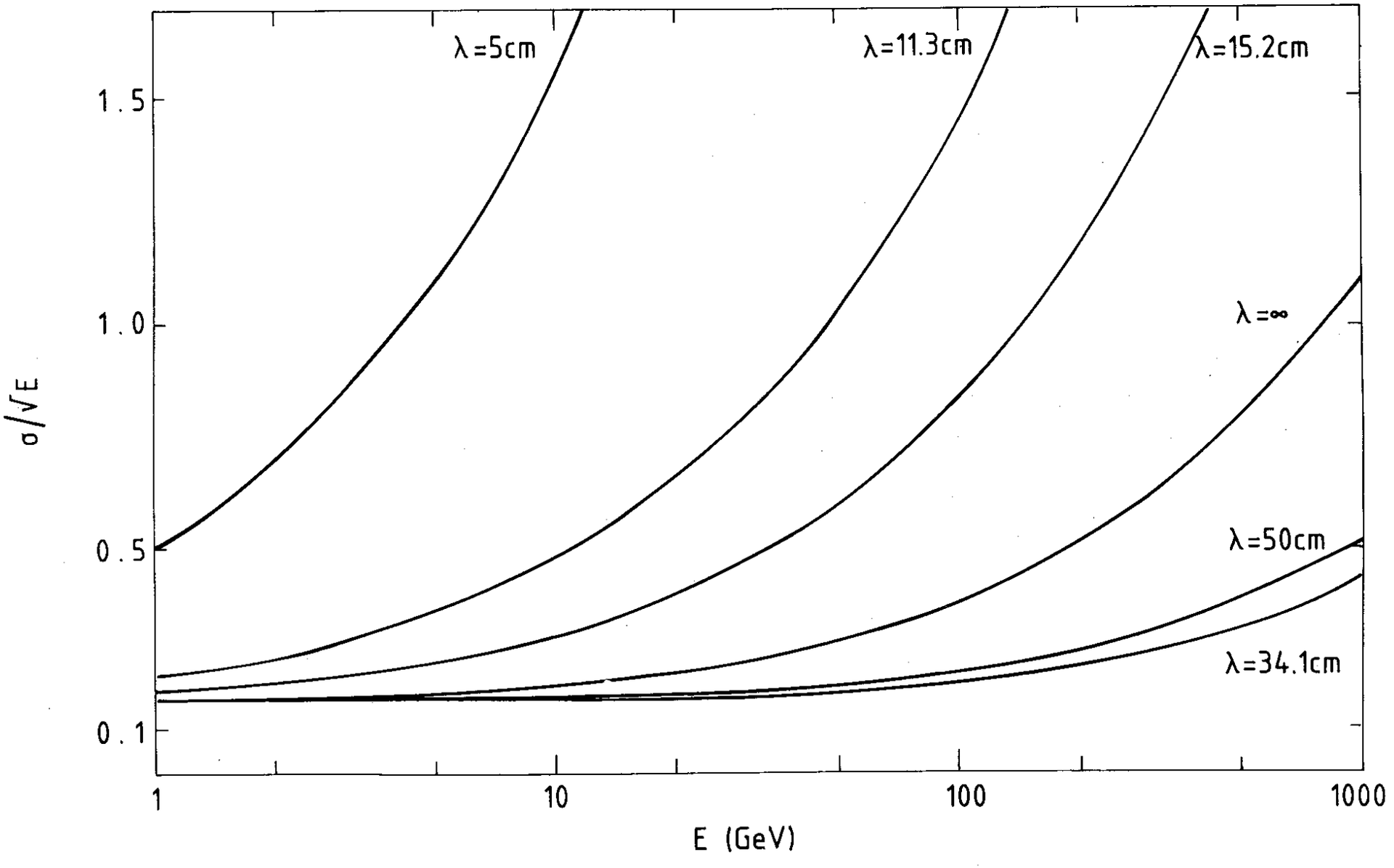
λ=5cm
λ=11.3cm
λ=15.2cm
λ=∞
λ=50cm
λ=34.1cm
1.5
1.0
0.5
0.1
σ/√E
1
10
100
1000
E (GeV)

Fig. 10a

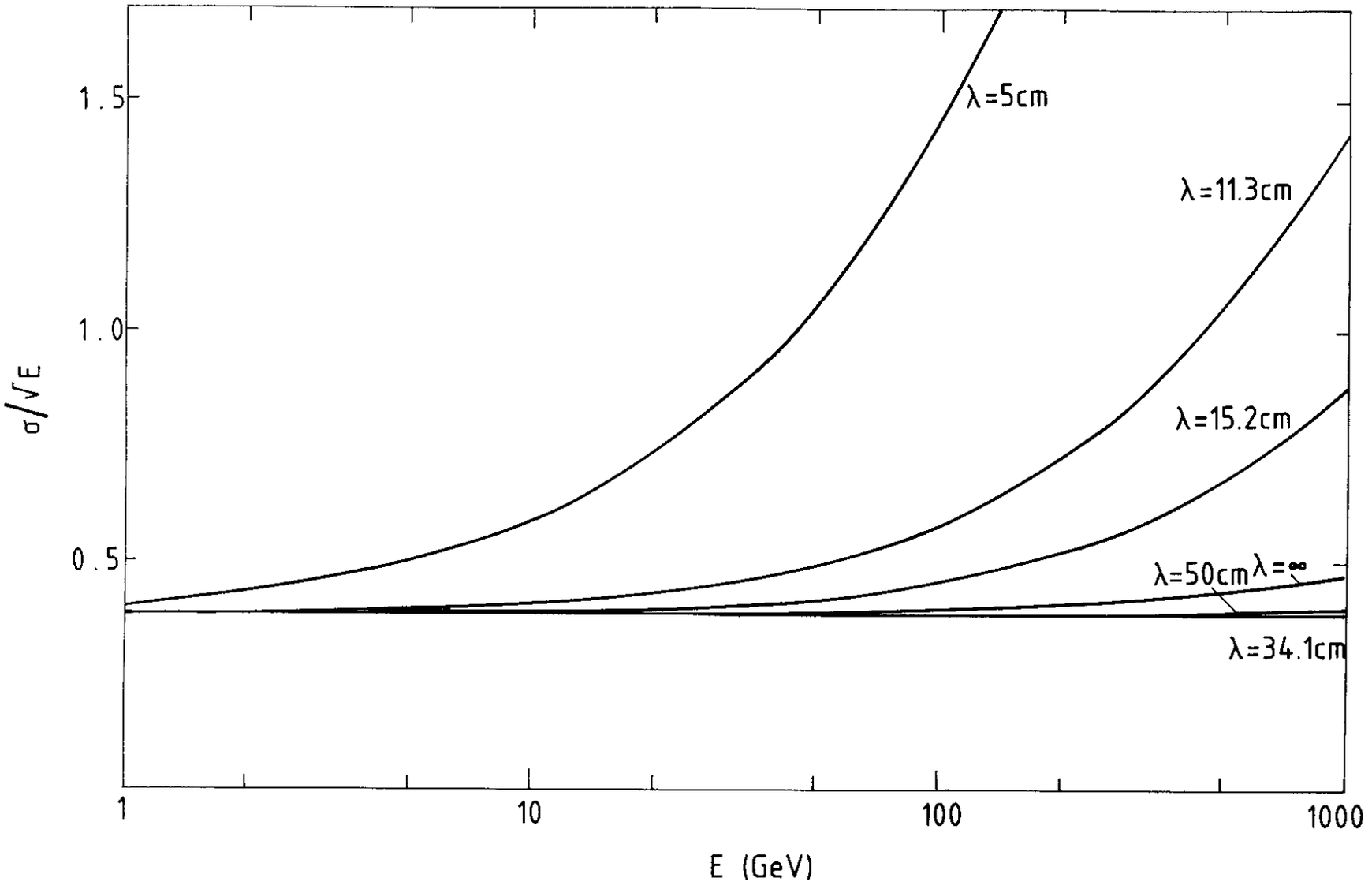
1.5
1.0
0.5
σ/√E
λ=5cm
λ=11.3cm
λ=15.2cm
λ=50cm
λ=∞
λ=34.1cm
1
10
100
1000
E (GeV)

Fig. 10b

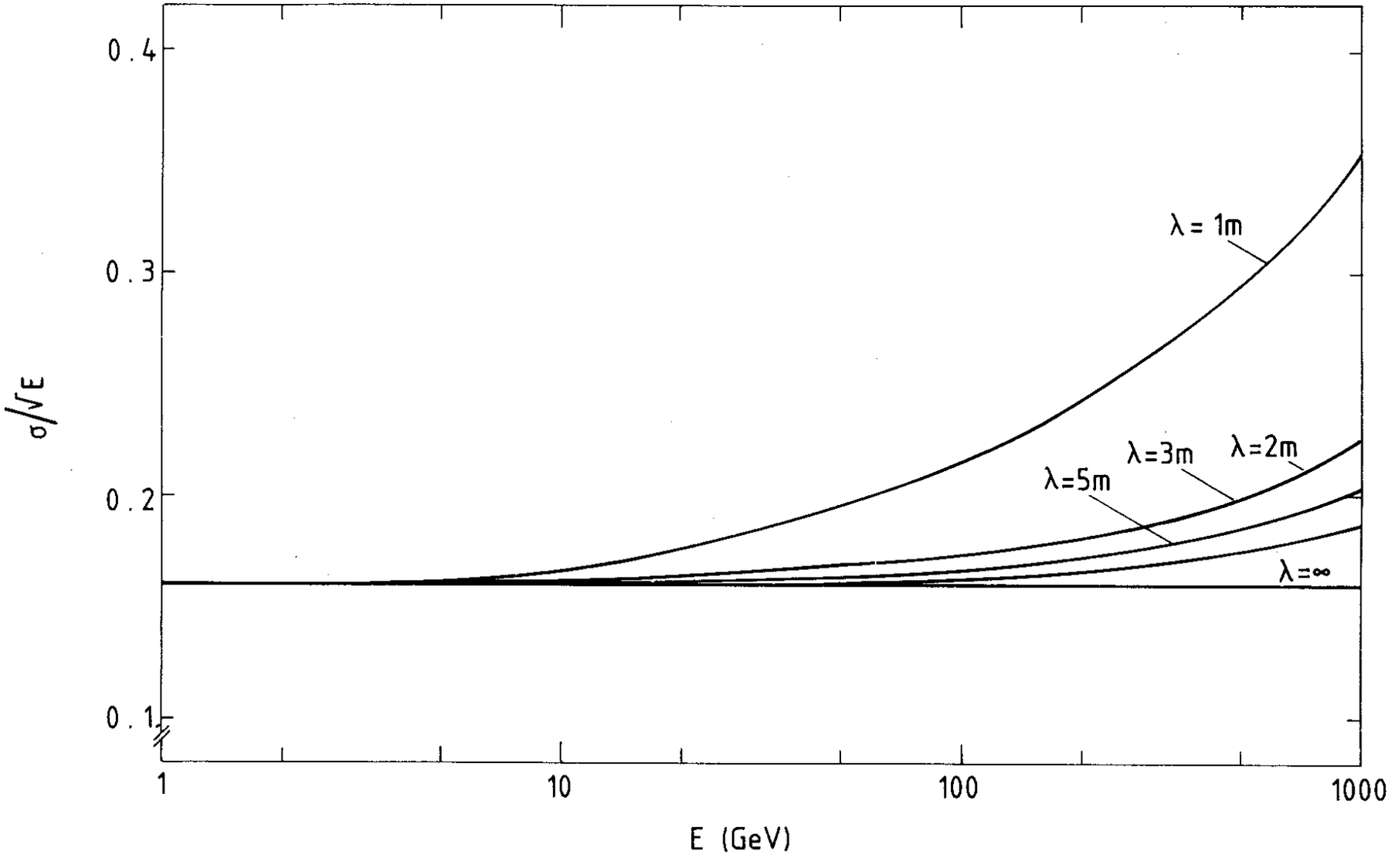

Fig. 11a

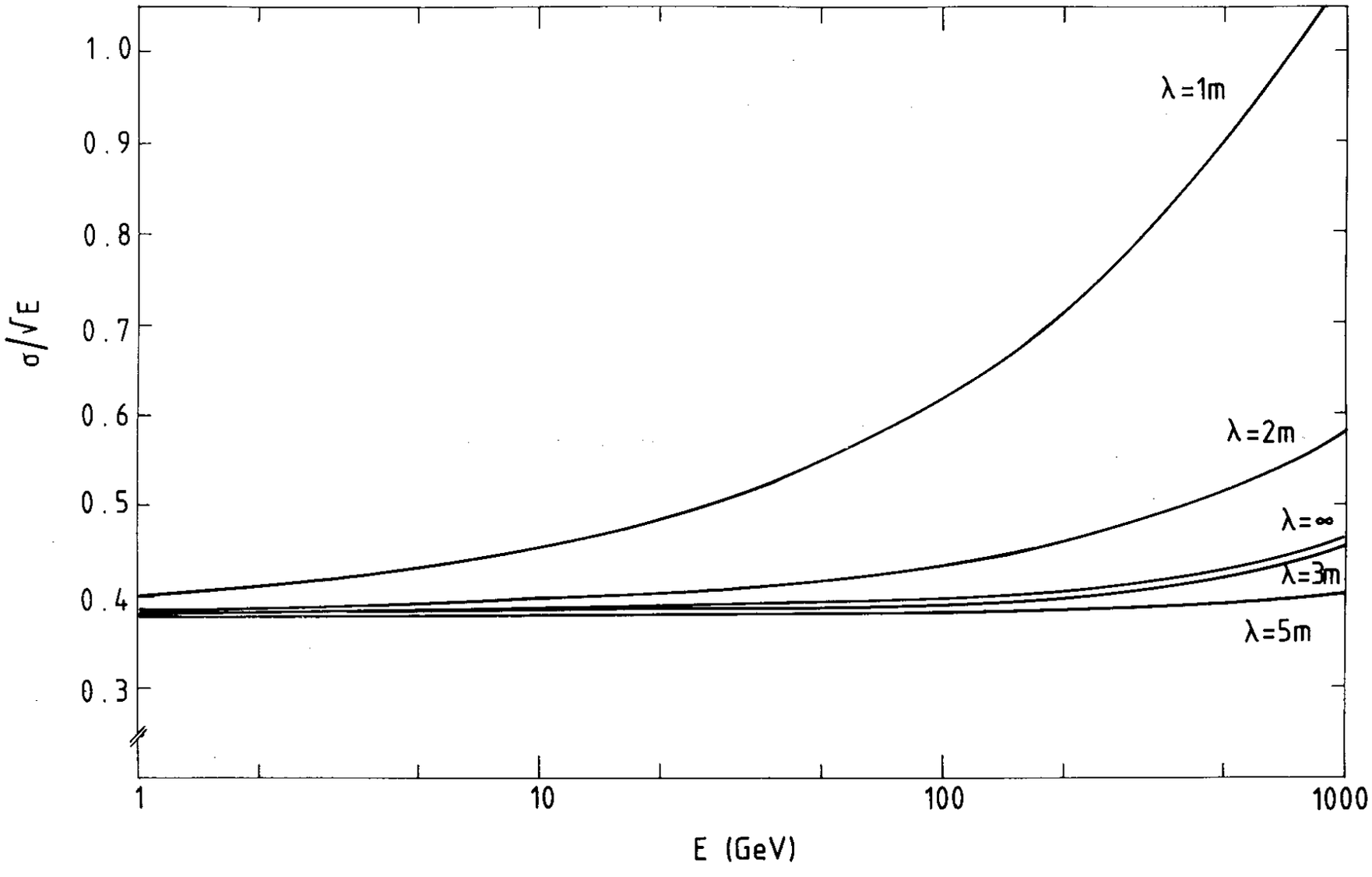

Fig. 11b

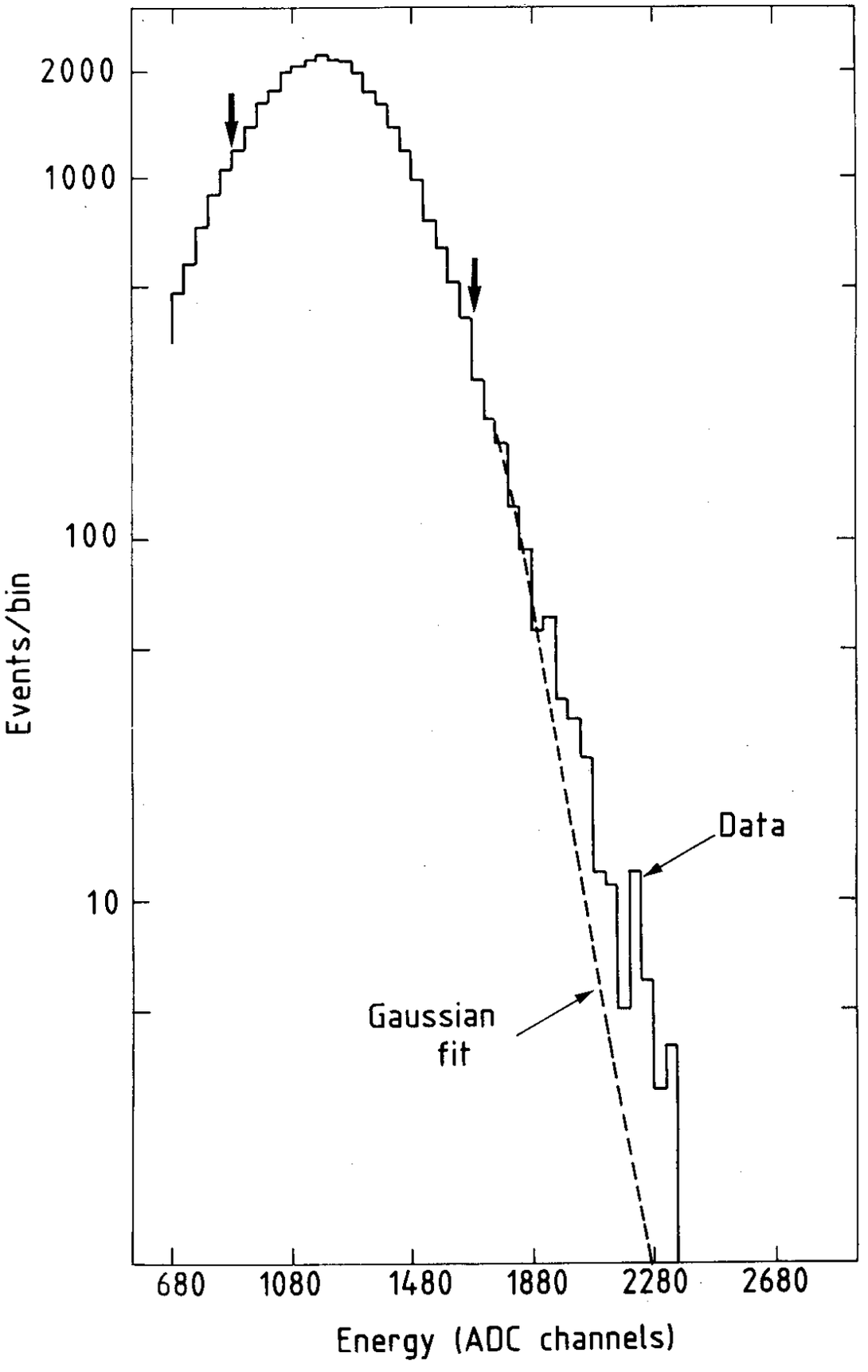
2000
1000
100
10
Events/bin
Data
Gaussian
fit
680
1080
1480
1880
2280
2680
Energy (ADC channels)

Fig. 12

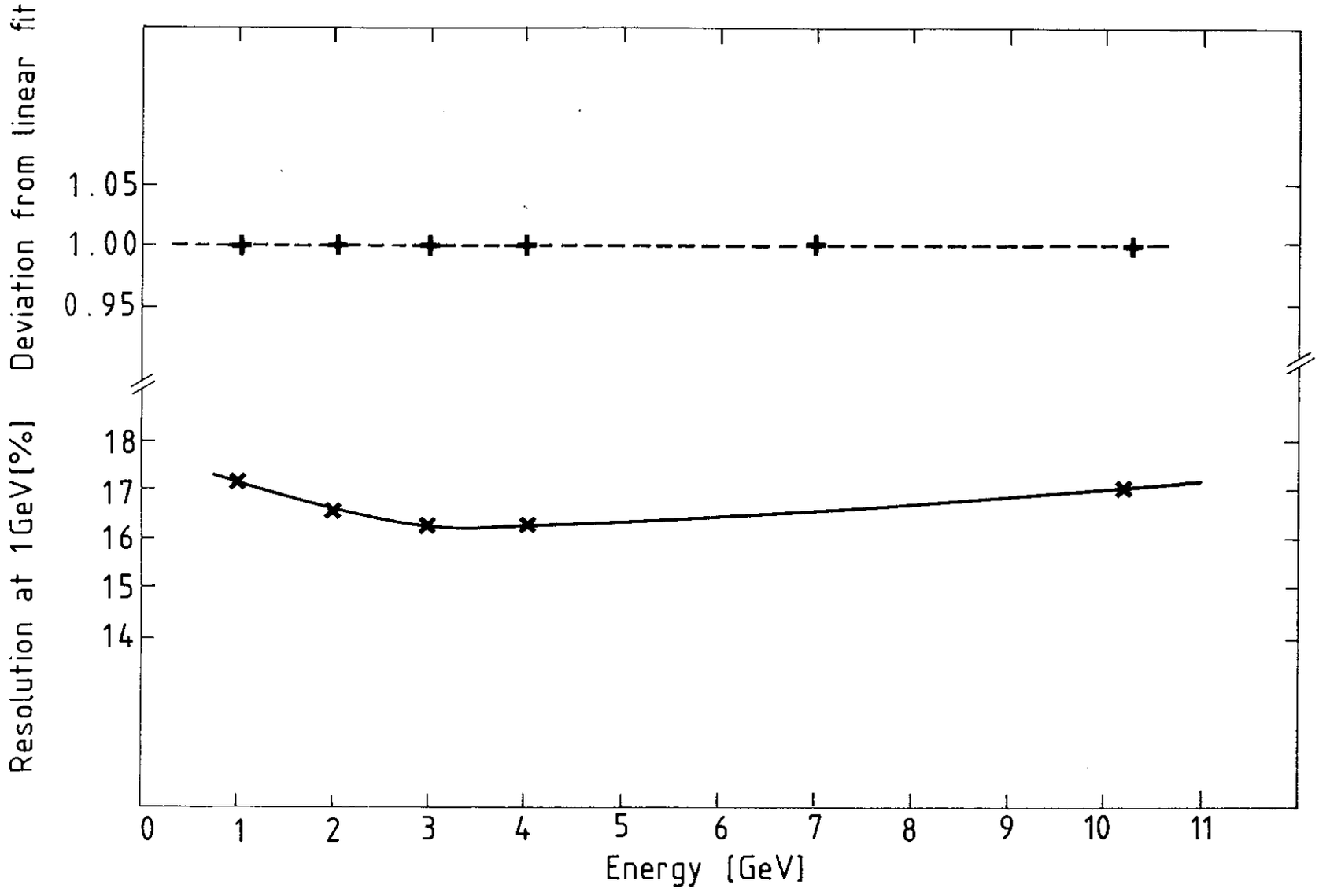
Deviation from linear fit
1.05
1.00
0.95
Resolution at 1GeV[%]
18
17
16
15
14
0
1
2
3
4
5
6
7
8
9
10
11
Energy [GeV]

Fig. 13

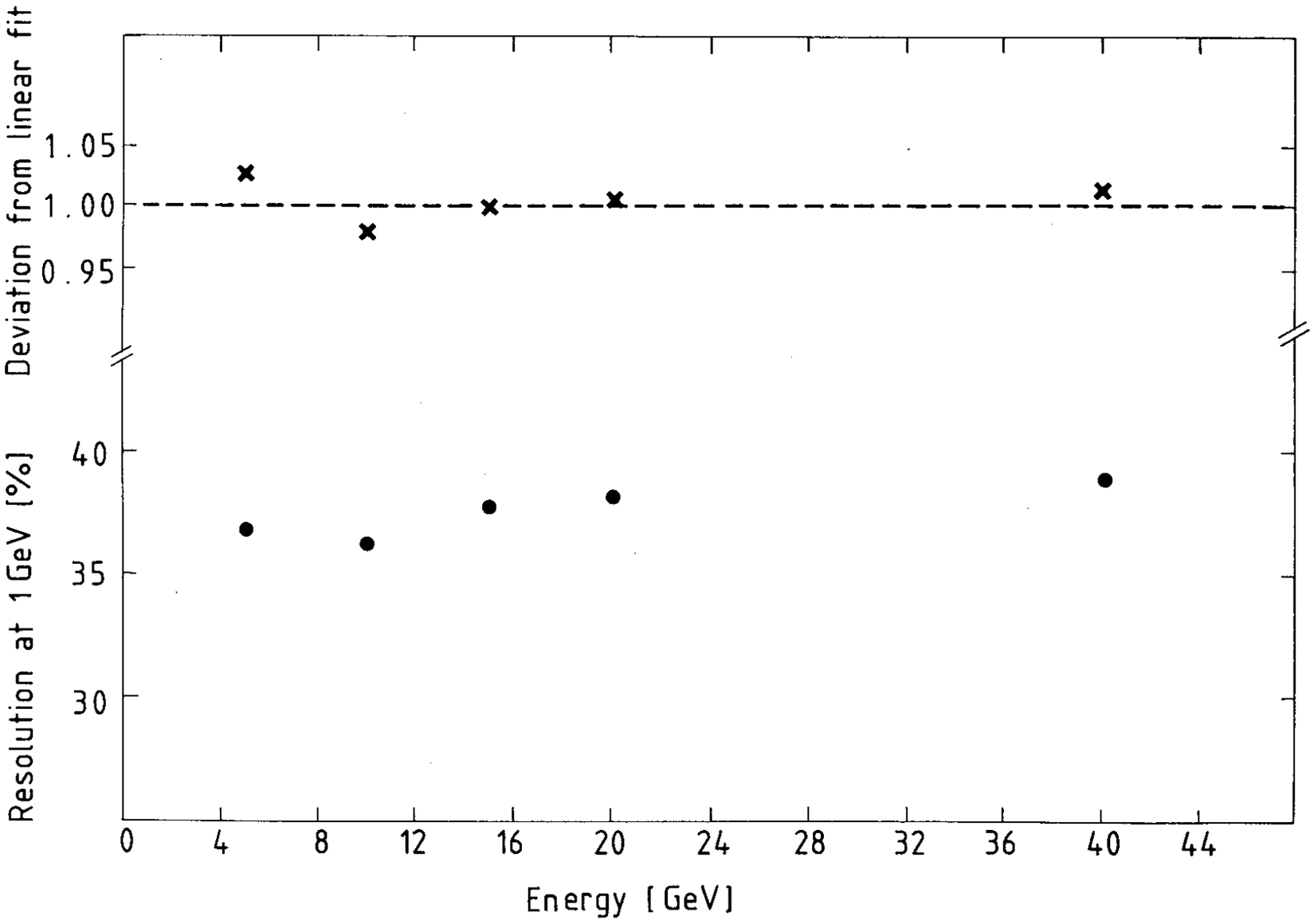
Deviation from linear fit
1.05
1.00
0.95
Resolution at 1 GeV [%]
40
35
30
0
4
8
12
16
20
24
28
32
36
40
44
Energy [GeV]

Fig. 14

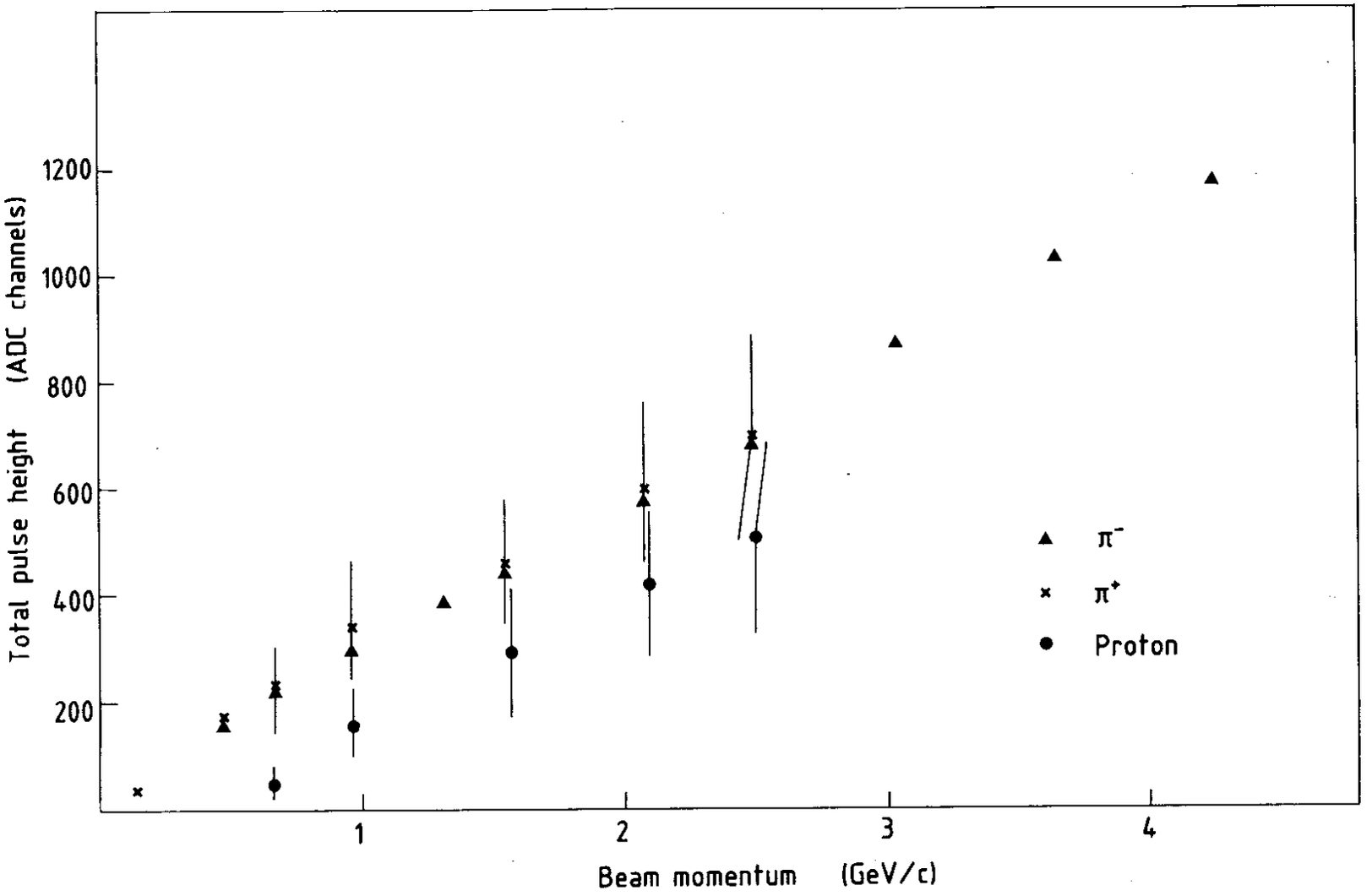
Total pulse height (ADC channels)
1200
1000
800
600
400
200
1
2
3
4
Beam momentum (GeV/c)
π⁻
π⁺
Proton

Fig. 15

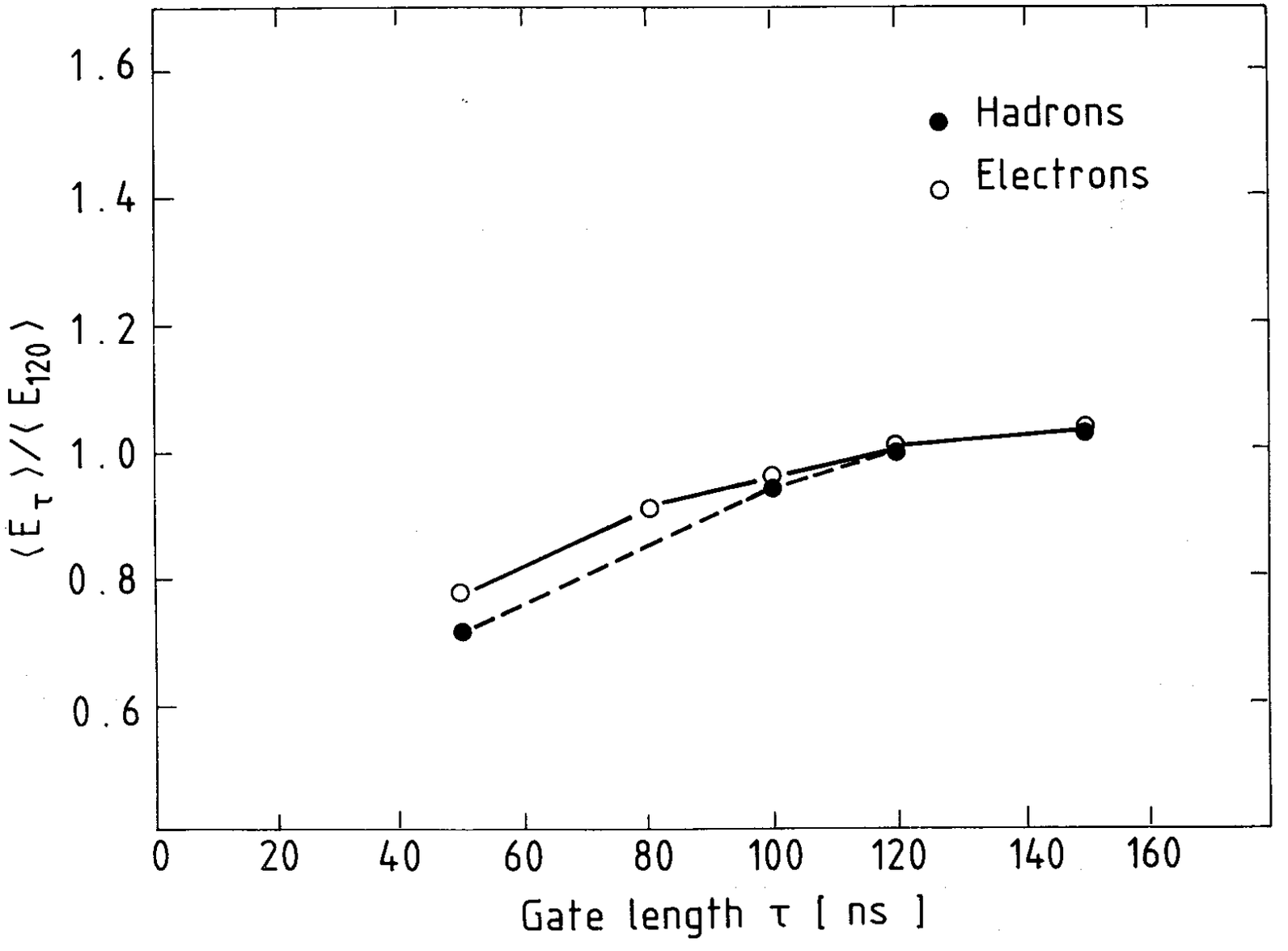
1.6
1.4
1.2
1.0
0.8
0.6
⟨Eτ⟩/⟨E120⟩
Hadrons
Electrons
0
20
40
60
80
100
120
140
160
Gate length τ [ns]

Fig. 16

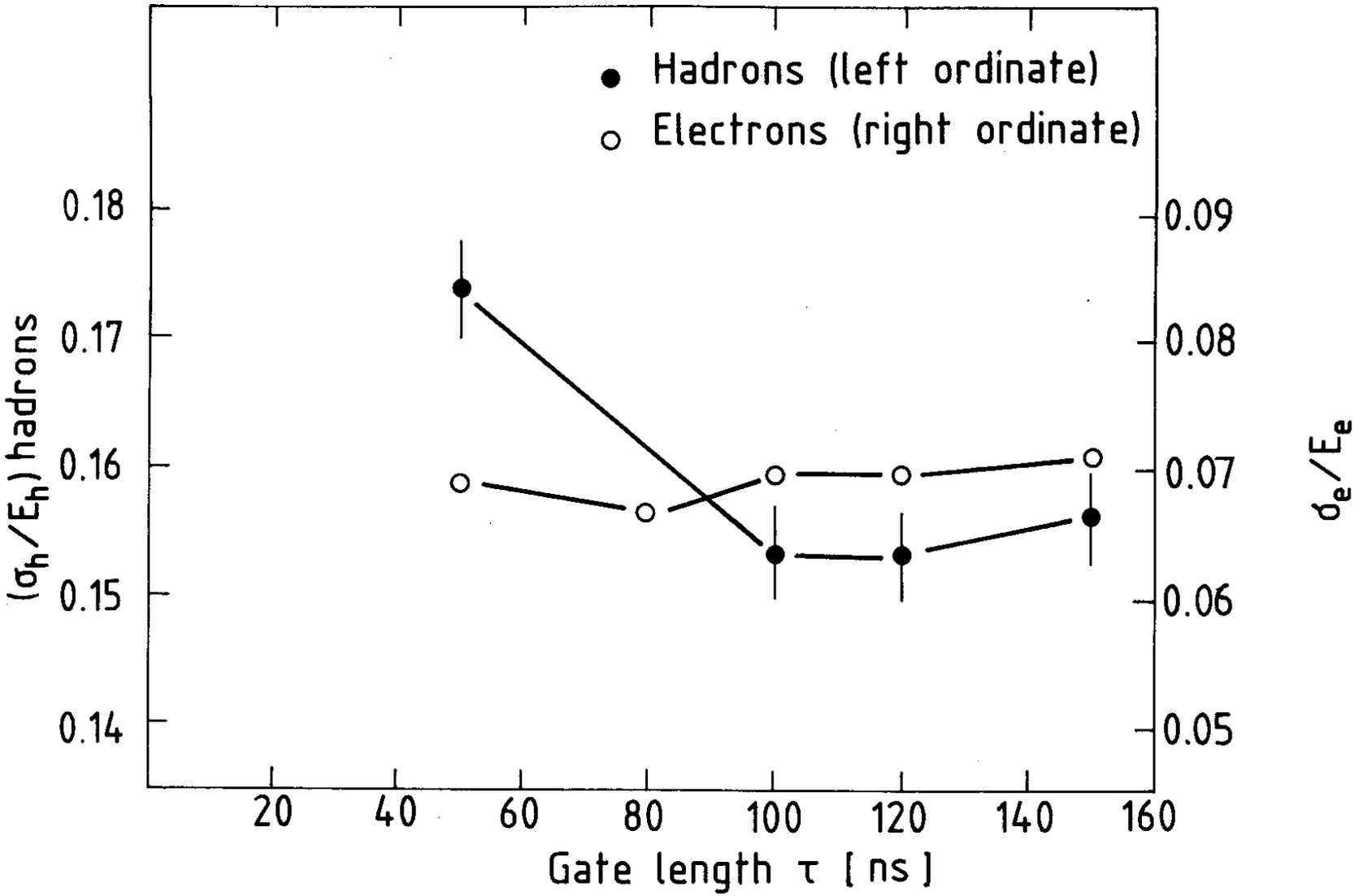
Hadrons (left ordinate)
Electrons (right ordinate)
0.18
0.17
0.16
0.15
0.14
0.09
0.08
0.07
0.06
0.05
20
40
60
80
100
120
140
160
Gate length τ [ns]
(σ_h/E_h) hadrons
σ_e/E_e

Fig. 17

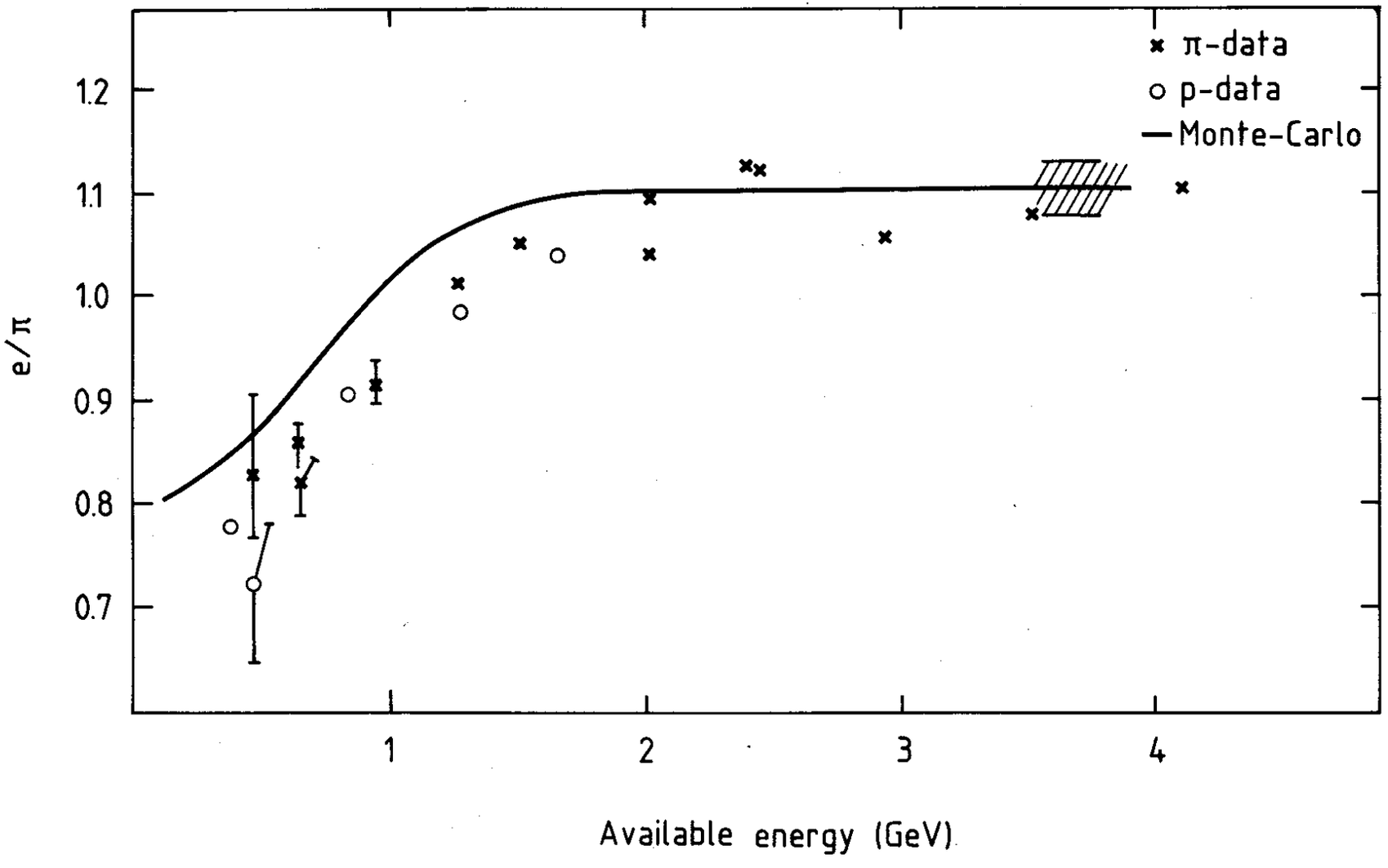
π-data
p-data
Monte-Carlo
e/π
1.2
1.1
1.0
0.9
0.8
0.7
1
2
3
4
Available energy (GeV)

Fig. 18

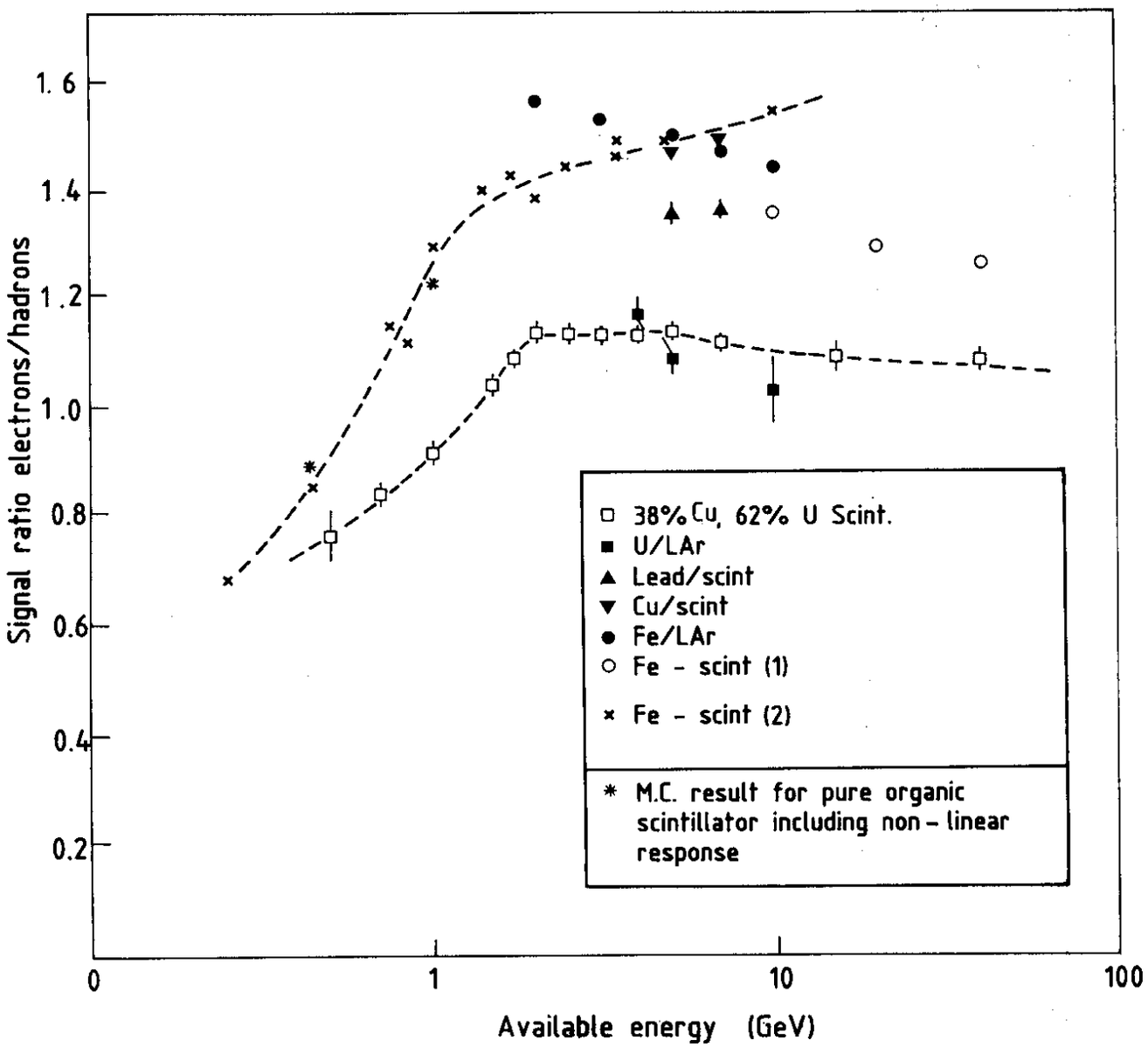
Signal ratio electrons/hadrons
1.6
1.4
1.2
1.0
0.8
0.6
0.4
0.2
0
1
10
100
Available energy (GeV)
38% Cu, 62% U Scint.
U/LAr
Lead/scint
Cu/scint
Fe/LAr
Fe - scint (1)
Fe - scint (2)
* M.C. result for pure organic scintillator including non - linear response

Fig. 19

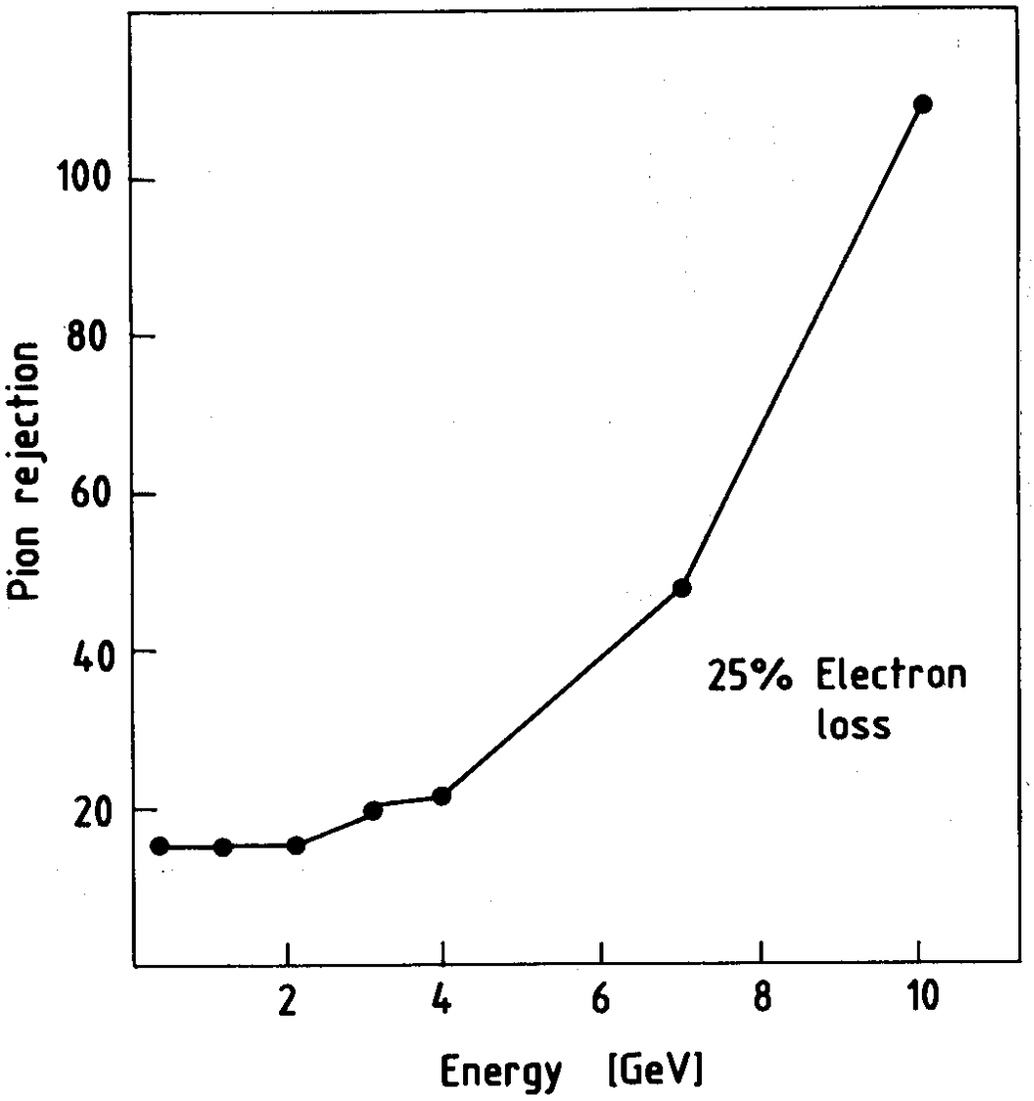
Pion rejection
100
80
60
40
20
2
4
6
8
10
Energy [GeV]
25% Electron
loss

Fig. 20

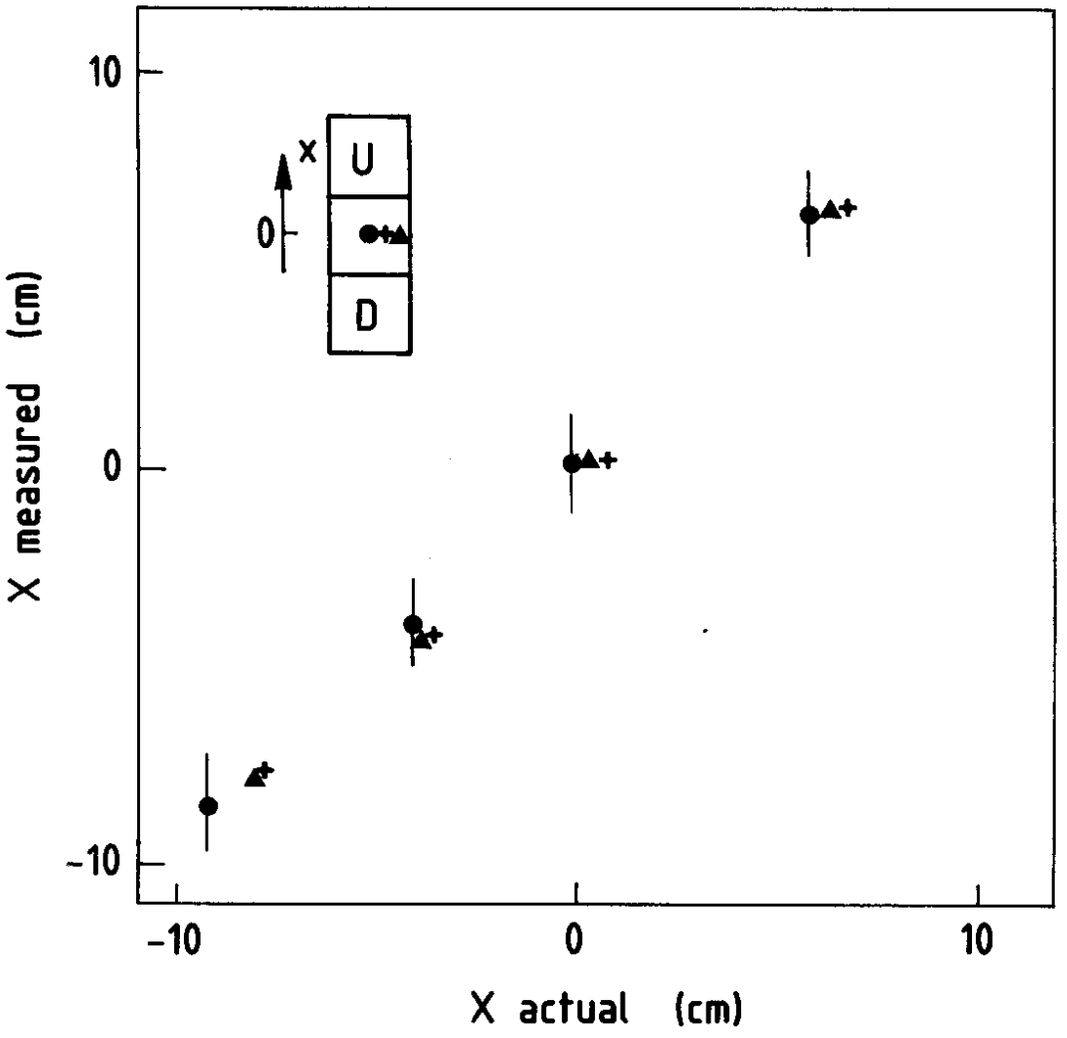

Fig. 21

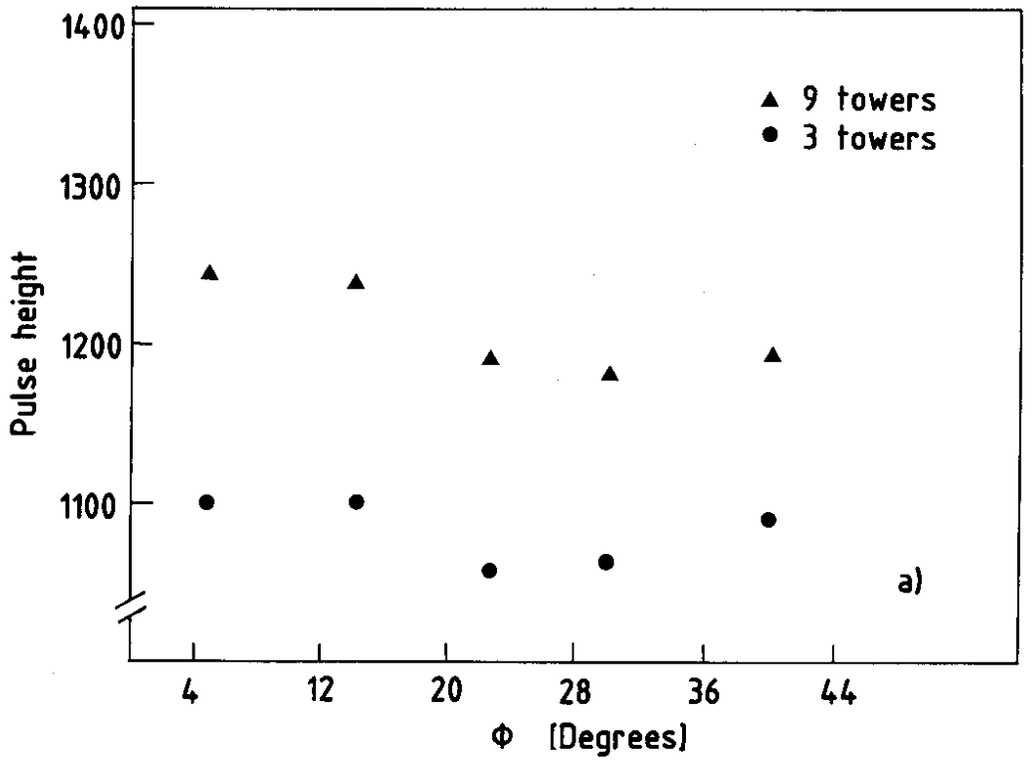
1400
1300
1200
1100
Pulse height
▲ 9 towers
● 3 towers
a)
4
12
20
28
36
44
Φ [Degrees]

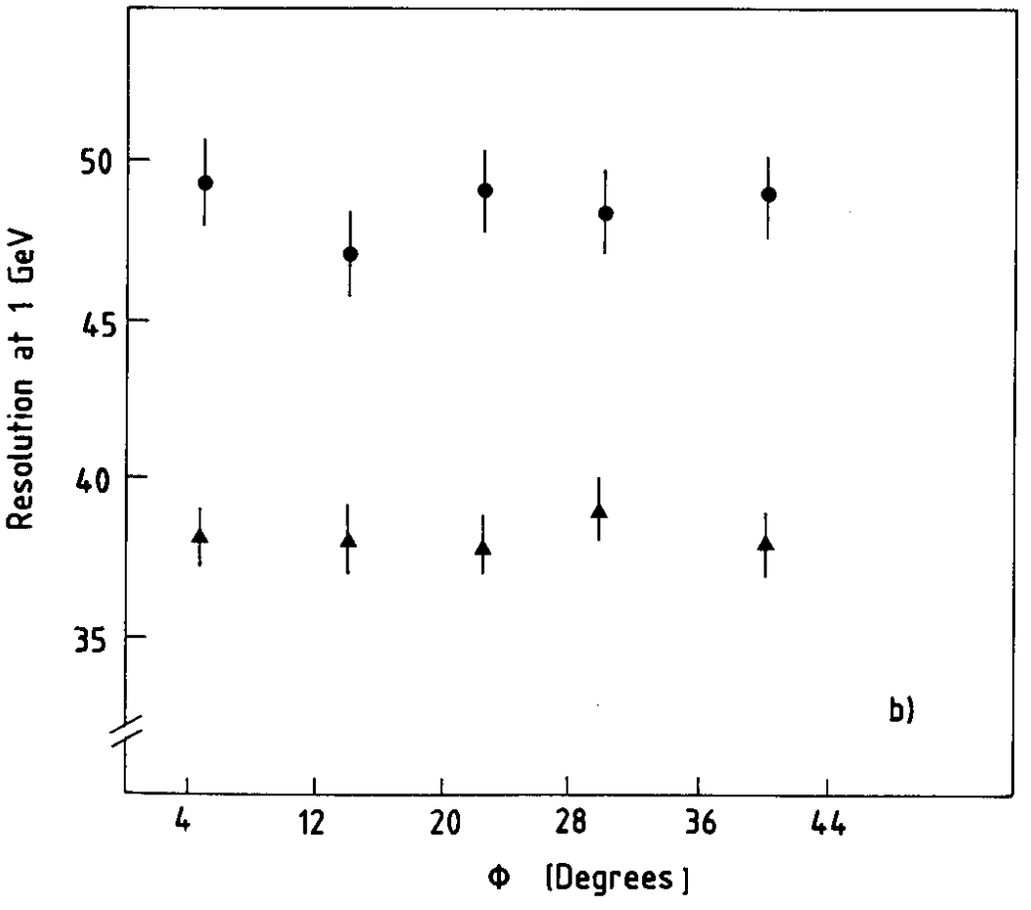
50
45
40
35
Resolution at 1 GeV
b)
4
12
20
28
36
44
Φ [Degrees]

Fig. 22

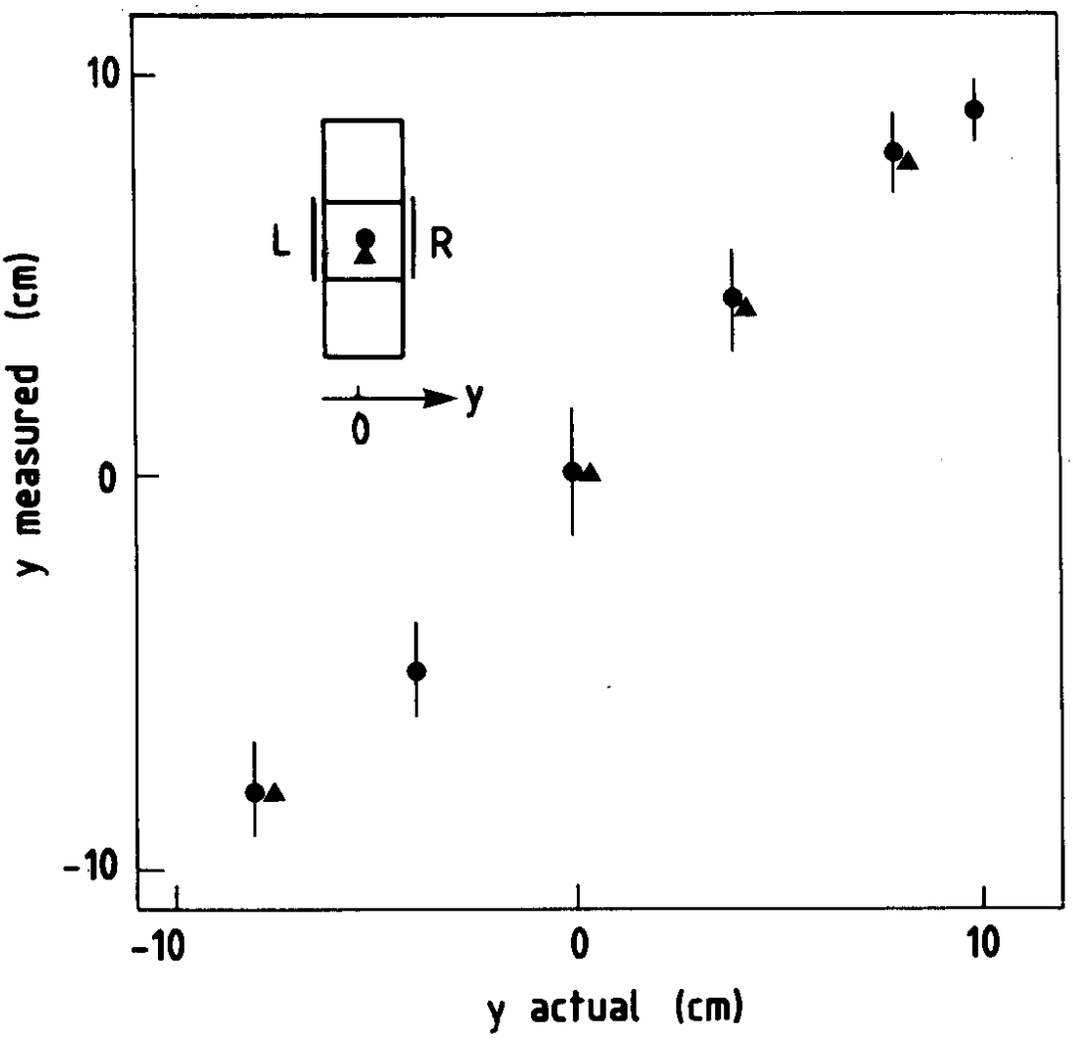

Fig. 23

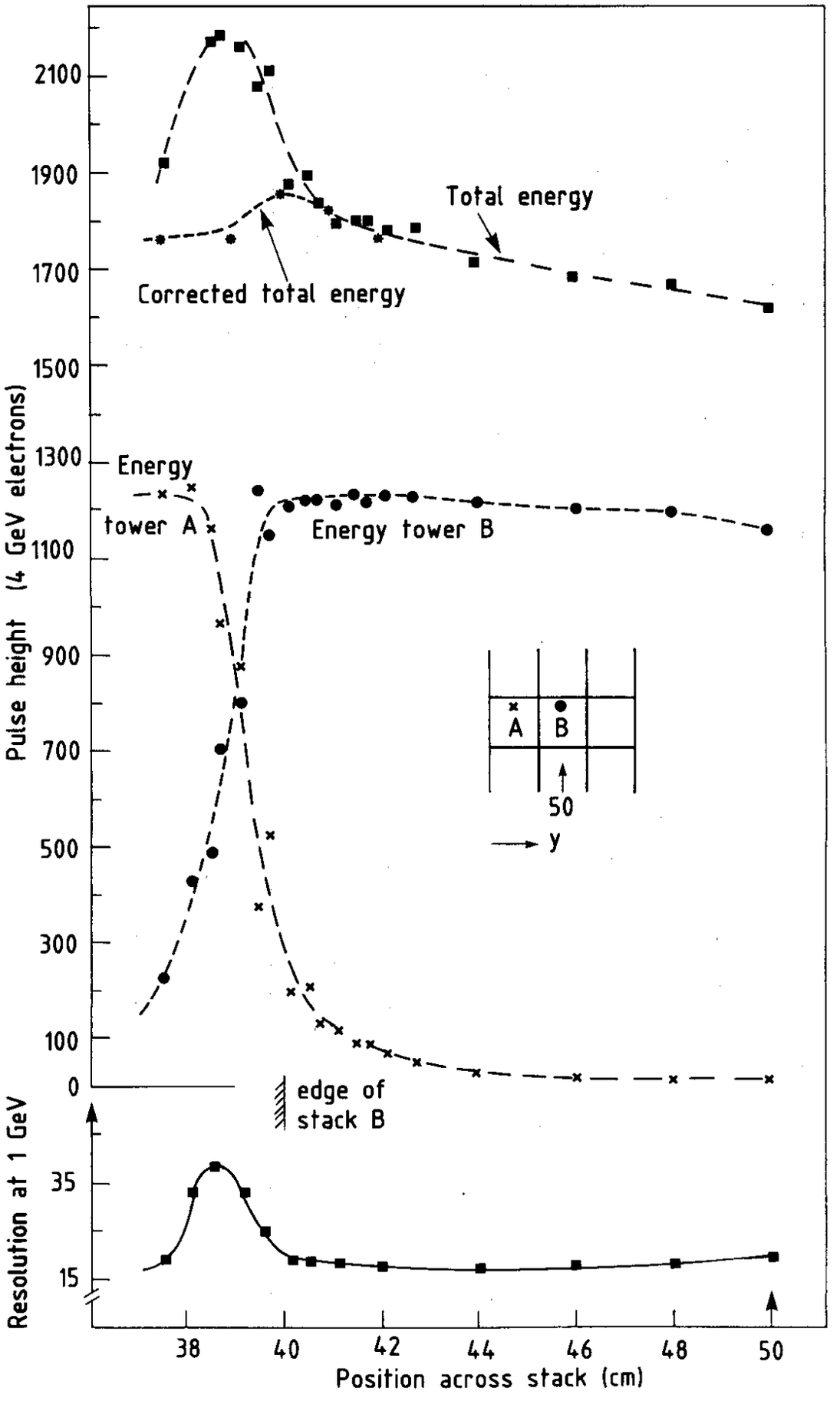
2100
1900
1700
1500
1300
1100
900
700
500
300
100
0
Pulse height (4 GeV electrons)
Total energy
Corrected total energy
Energy tower A
Energy tower B
A
B
50
y
edge of stack B
35
15
Resolution at 1 GeV
38
40
42
44
46
48
50
Position across stack (cm)

Fig. 24

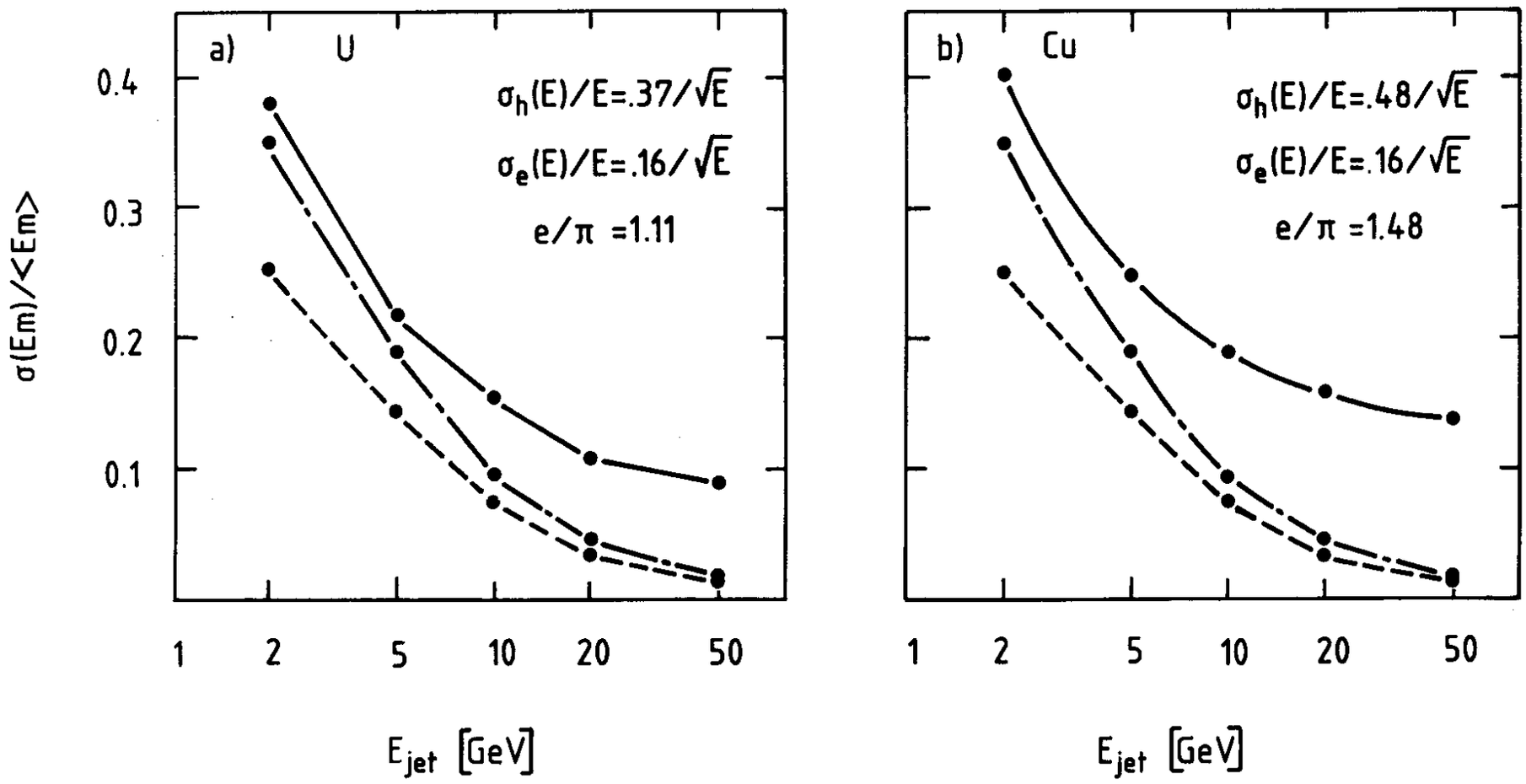
a)
U
$\sigma_h(E)/E=.37/\sqrt{E}$
$\sigma_e(E)/E=.16/\sqrt{E}$
e/π =1.11
b)
Cu
$\sigma_h(E)/E=.48/\sqrt{E}$
$\sigma_e(E)/E=.16/\sqrt{E}$
e/π =1.48
σ(Em)/<Em>
0.4
0.3
0.2
0.1
1
2
5
10
20
50
E_{jet} [GeV]

Fig. 25

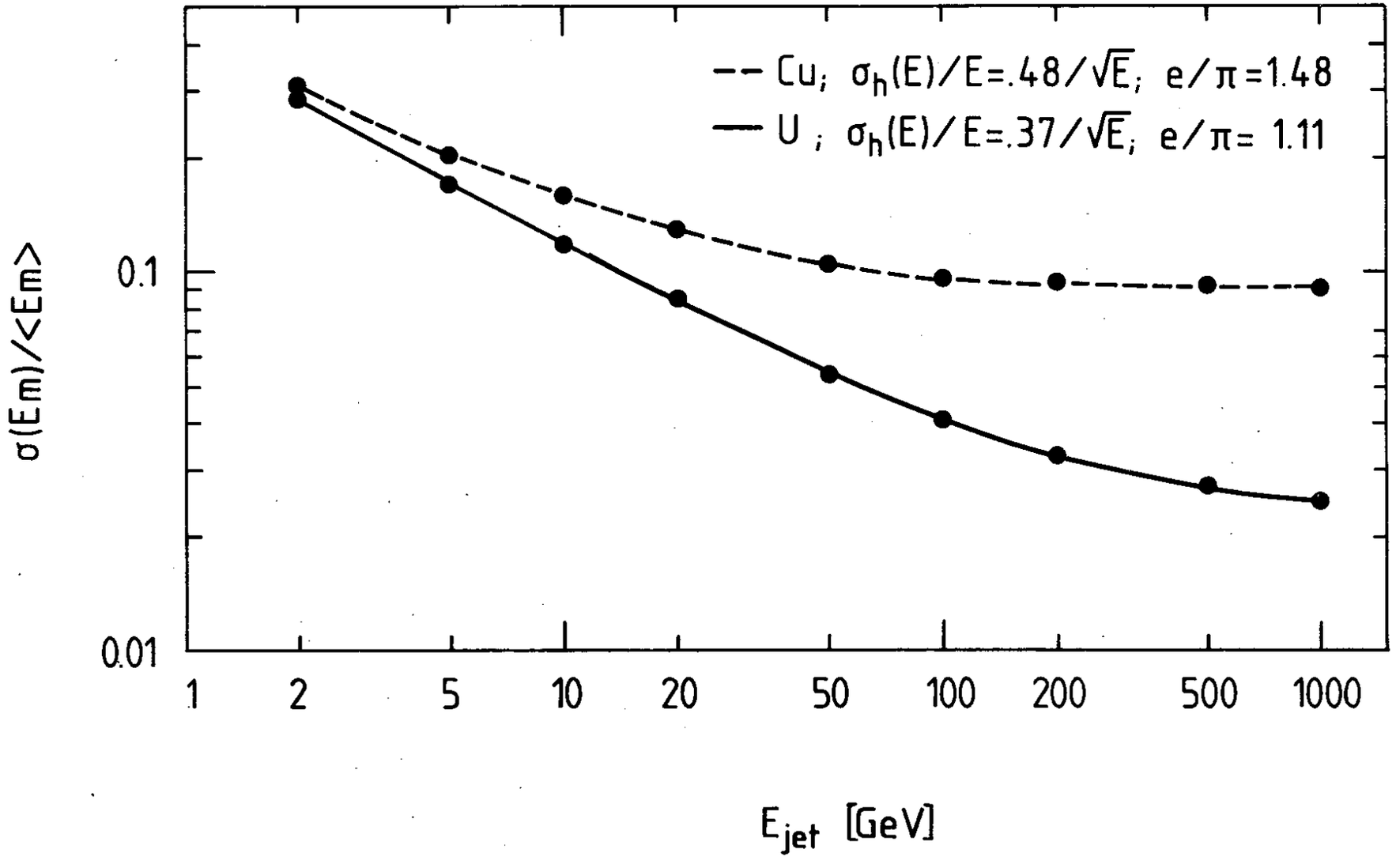
-- Cu; $\sigma_h(E)/E=.48/\sqrt{E}$; $e/\pi=1.48$
— U ; $\sigma_h(E)/E=.37/\sqrt{E}$; $e/\pi=1.11$
$\sigma(Em)/<Em>$
0.1
0.01
1
2
5
10
20
50
100
200
500
1000
E_{jet} [GeV]

Fig. 26

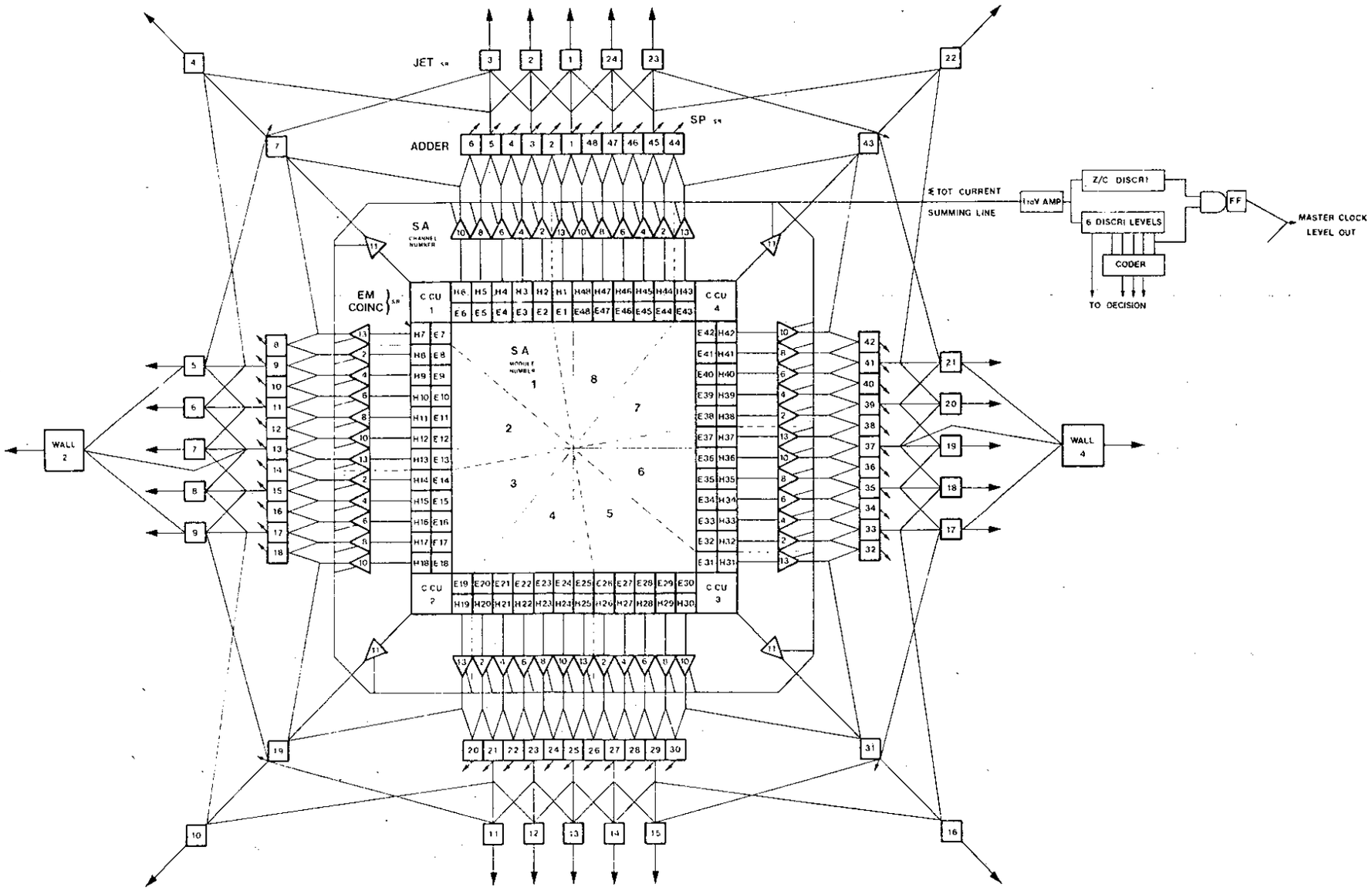
JET
SP
ADDER
Σ TOT CURRENT
SUMMING LINE
Z/C DISCRI
6 DISCRI LEVELS
CODER
FF
MASTER CLOCK
LEVEL OUT
TO DECISION
SA
EM
COINC
CCU 1
CCU 2
CCU 3
CCU 4
WALL 2
WALL 4

Fig. 27

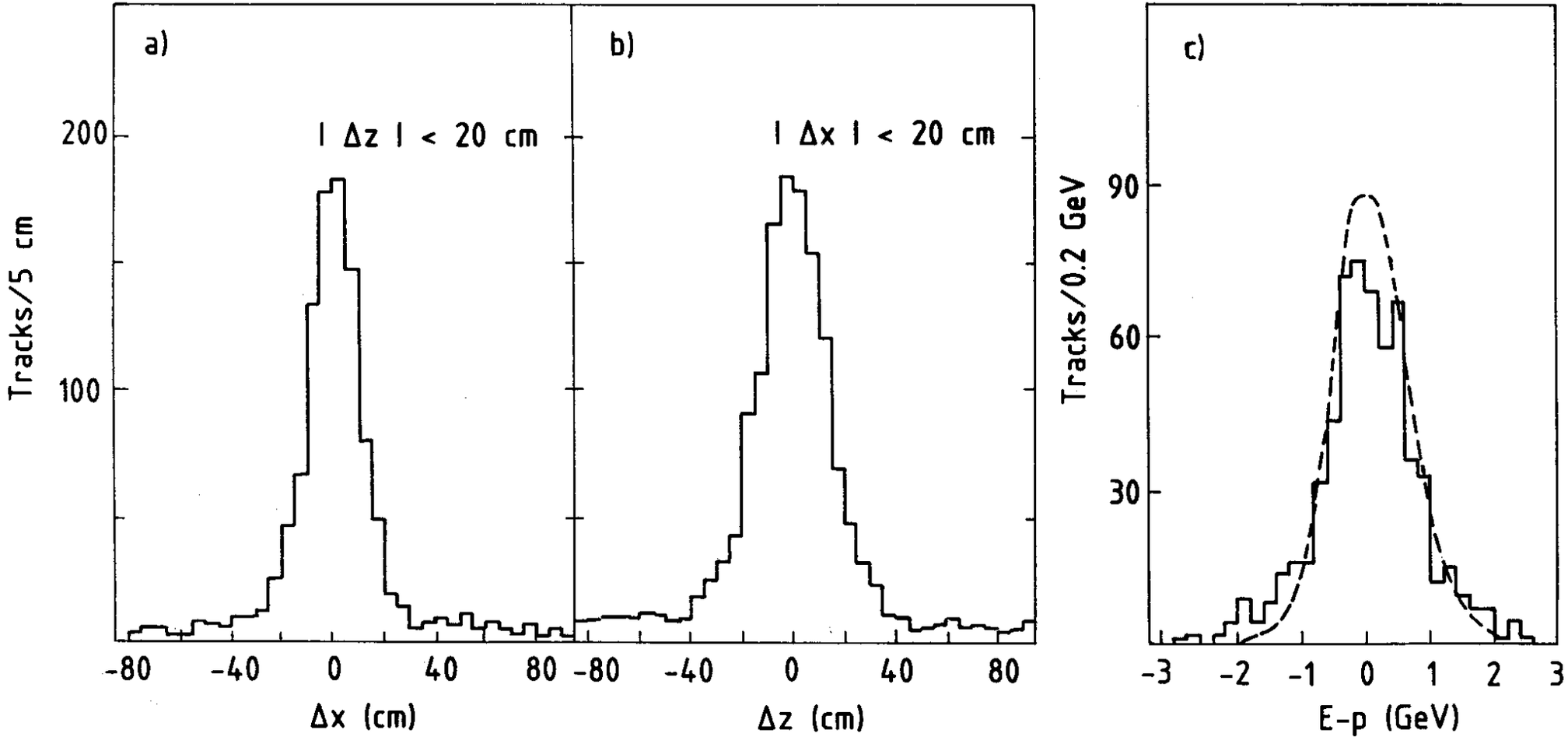
a)
b)
c)
| Δz | < 20 cm
| Δx | < 20 cm
Tracks/5 cm
Tracks/0.2 GeV
200
100
90
60
30
-80
-40
0
40
80
-3
-2
-1
1
2
3
Δx (cm)
Δz (cm)
E-p (GeV)

Fig. 28

A F S

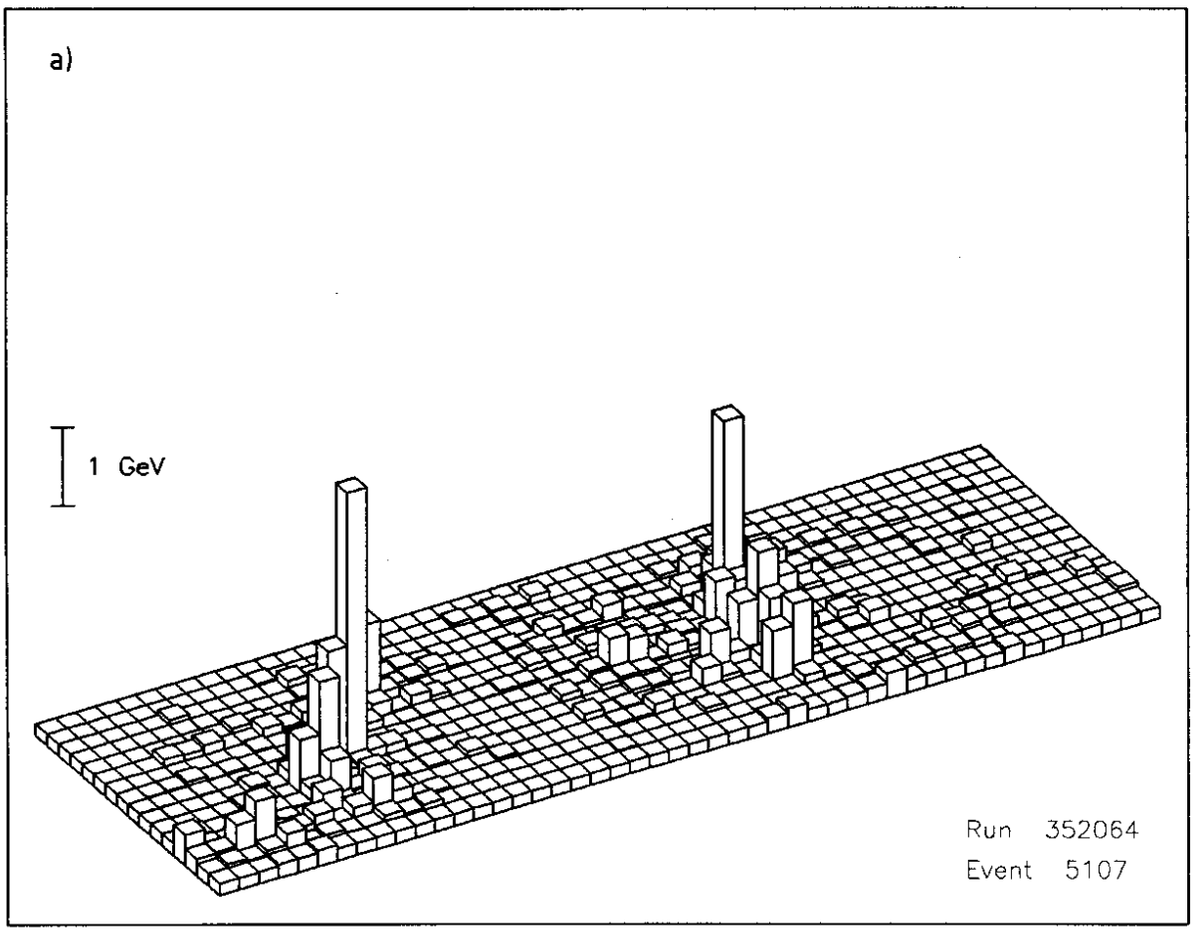

A F S

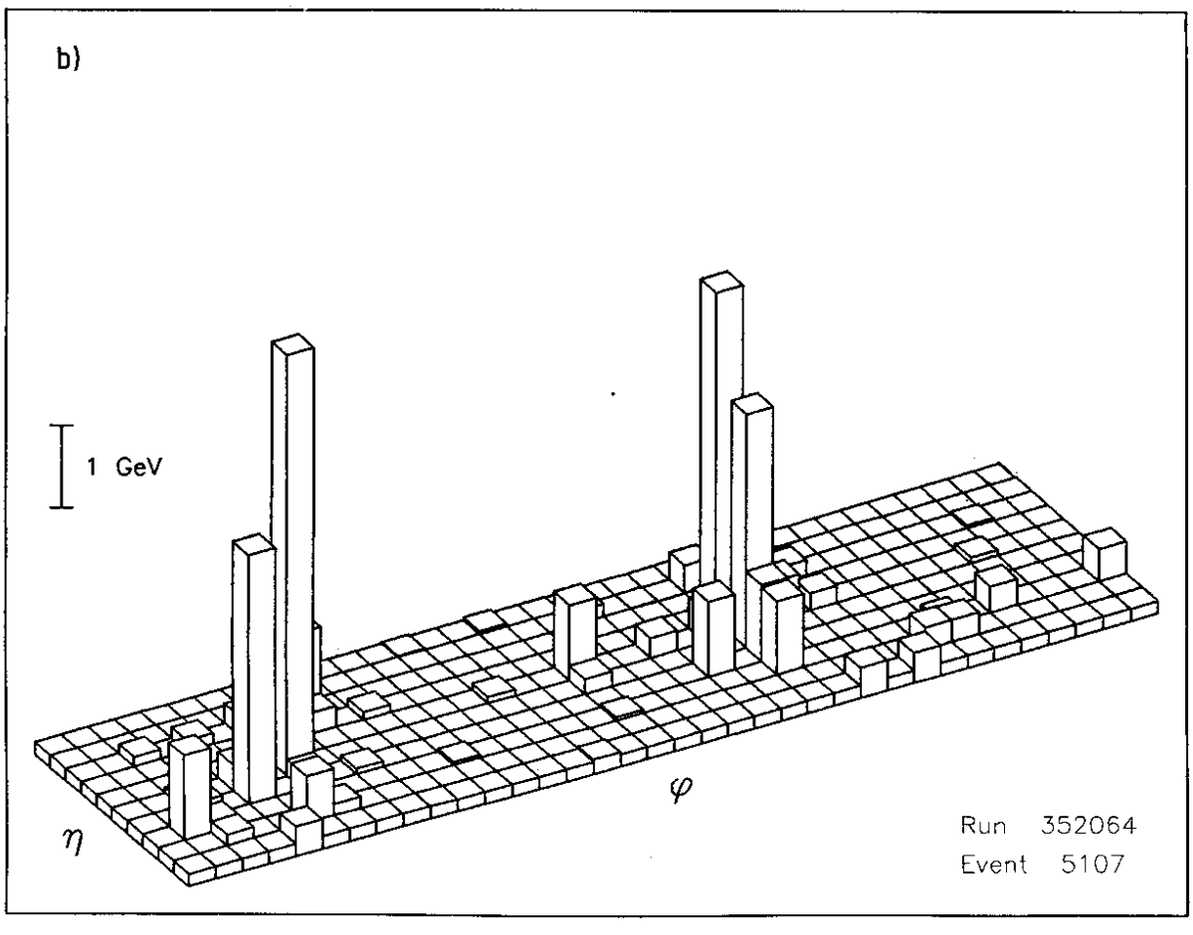

Fig. 29

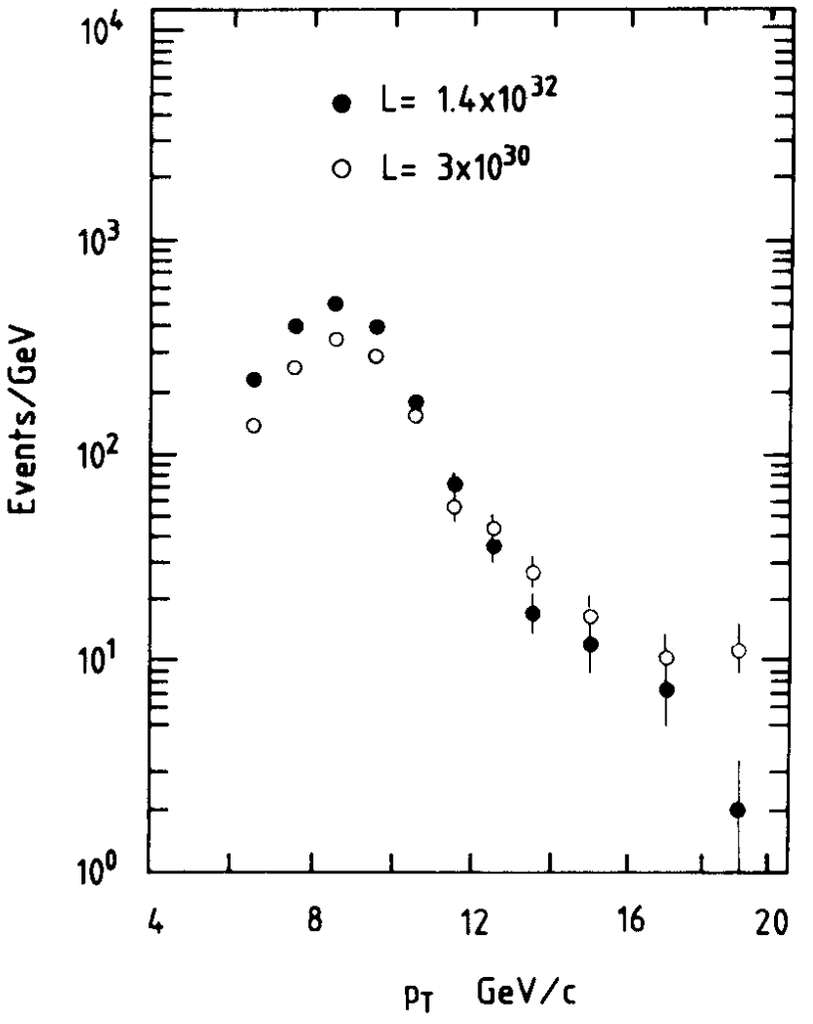
10^4
10^3
10^2
10^1
10^0
Events/GeV
L= 1.4x10^{32}
L= 3x10^{30}
4
8
12
16
20
p_T GeV/c

Fig. 30